

Implementation and assessment of a model including mixotrophs and the carbonate cycle (Eco3M_MIX-CarbOx v1.0) in a highly dynamic Mediterranean coastal environment (Bay of Marseille, France) (Part. II): Towards a better representation of total alkalinity
5 **when modelling the carbonate system and air-sea CO₂ fluxes**

Lucille Barré¹, Frédéric Diaz^{1,†}, Thibaut Wagener¹, Camille Mazoyer¹, Christophe Yohia² and Christel Pinazo¹

¹Aix Marseille Univ., Université de Toulon, CNRS, IRD, MIO, UM 110, 13288, Marseille, France

²Aix Marseille Univ., Université de Toulon, CNRS, IRD, OSU Institut Pythéas, 13288, Marseille France

10 [†]Deceased

Correspondence to: Lucille Barré (lucille.barre@mio.osupytheas.fr), Thibaut Wagener (thibaut.wagener@mio.osupytheas.fr)

Abstract

The Bay of Marseille (BoM), located in the north-western Mediterranean Sea, is affected by various hydrodynamic processes (e.g., Rhône River intrusion and upwelling events) that result in a highly complex local carbonate system. In any complex environment, the use of models is advantageous since it allows to identify the different environmental forcings, thereby facilitating a better understanding. By combining approaches from two biogeochemical ocean models and improving the formulation of total alkalinity, we develop a more realistic representation of the carbonate system variables at high temporal resolution which enables us study air-sea CO₂ fluxes and seawater *p*CO₂ variations more reliably. We apply this new formulation to two particular scenarios, typical for the BoM: (i) summer upwelling and (ii) Rhône River intrusion events. In both scenarios, our model was able to correctly reproduce the observed patterns of *p*CO₂ variability. Summer upwelling events are typically associated with *p*CO₂ decrease that mainly results from decreasing near-surface temperatures. Furthermore, Rhône River intrusion events are typically associated with *p*CO₂ decrease, although in this case the *p*CO₂ decrease results from a decrease in salinity and an overall increase in total alkalinity. While our model was able to correctly represent the daily range of air-sea CO₂ fluxes, we were unable to correctly estimate the yearly total air-sea CO₂ flux. Although the model - consistent with observations - predicted the BoM to be a sink of CO₂ on a yearly basis, the magnitude of this CO₂ sink was underestimated which may be an indication of the limitations inherent in dimensionless models for representing air-sea CO₂ fluxes.

Keywords: Carbonate system, Bay of Marseille, Total alkalinity, Air-sea CO₂ fluxes, Modelling, Acidification

1 Introduction

Since the industrial revolution, atmospheric CO₂ concentrations have constantly increased (Mauna Loa Observatory: <https://gml.noaa.gov/ccgg/trends/>). By absorbing large amounts of CO₂, the global ocean acts as an important sink of anthropogenic CO₂. Recent estimates suggest that this absorption corresponds to roughly 25 % of annual emissions (Friedlingstein et al., 2022). During this absorption process, CO₂ undergoes a series of acid-base reactions that eventually lead to the formation of carbonate ions (CO₃²⁻). Initially, dissolved CO₂ reacts with water to form carbonic acid (H₂CO₃) which then, dissociates into bicarbonate (HCO₃⁻) and hydronium (H⁺) ions. In turn, HCO₃⁻ dissociates into CO₃²⁻ and H⁺ ions. Increased uptake of atmospheric CO₂ modifies this acid-base reaction chain, thus affecting the associated species concentrations, particularly of H⁺ ions which increase significantly resulting in a decrease in seawater pH. This phenomenon, known as ocean acidification (OA), is ubiquitous as confirmed through global observations (Feely et al., 2009; Dore et al., 2009; Gonzales-Dávila et al., 2010; Bates et al., 2012). The increased uptake of atmospheric CO₂ not only results in lower pH but also modifies the overall carbonate equilibrium which is slowly shifting toward higher HCO₃⁻ and H₂CO₃ concentrations and lower CO₃²⁻ concentrations, which makes it more difficult for marine calcifiers to form their calcium carbonate shells (Orr et al., 2005).

Coastal oceans (depth < 200 m, Gattuso et al., 1998) accounts for over 10 % (0.18 to 0.45 PgC per year, Laruelle et al., 2010;

2014) of the total oceanic CO₂ uptake (Thomas et al., 2004) and are therefore particularly impacted by OA, generally exhibiting more pronounced localized decreases in pH (e.g., Kapsenberg et al., 2017; Luchetta et al., 2010). Nonetheless, coastal environments are highly complex mainly due to their high spatial and temporal variability, which makes their response to changes difficult to predict (Carstensen et al., 2018). Their proximity to the land means they are particularly exposed to anthropogenic pressures (run off and riverine input of anthropogenic nutrients and other chemical products, and organic matter rejects). Moreover, they are affected by strong physical forcings (e.g., tides, salinity gradients, wind induced currents) and account for about 30 % of all oceanic primary production which typically results in rich and diverse ecosystems (Gattuso et al., 1998).

The Mediterranean Sea is comparatively small and semi-enclosed; it receives nutrients through several pathways including Saharan dust depositions (Guerzoni et al., 1997) and numerous riverine inputs (e.g., Hopkins, 1992; Salat et al., 2002; Pujopay et al., 2006). Considering that the Mediterranean Sea is mostly oligotrophic (Morel & Andre, 1991), these inputs are highly significant for phytoplankton growth (Revelante & Gillmartin, 1976; Ludwig et al., 2009). These features render the biogeochemistry of the Mediterranean Sea particularly complex, especially regarding the carbonate system. Several studies have investigated the carbonate system and air-sea CO₂ fluxes in these areas, typically using point measurements from various locations including, the Ligurian Sea (De Carlo et al., 2013; Kapsenberg et al., 2017), the Bay of Marseille (BoM; Wimart-Rousseau et al., 2020), the Gulf of Trieste (Ingrosso et al., 2016) and the Adriatic Sea (Urbini et al., 2020). Overall, these studies agree with findings by Roobaert et al. (2019) who showed that coastal systems mostly act like CO₂ sinks on a yearly basis, although the CO₂ uptake shows a significant intra-annual variability.

Most modelling approaches to investigate carbonate system variables typically employ 3D coupled physical-biogeochemical models and focus on larger coastal areas (e.g., Artioli et al., 2014; Bourgeois et al., 2016). If the focus is on smaller areas this requires higher spatial and temporal resolution to correctly represent the relevant processes (Bourgeois et al., 2016). However, higher spatial and temporal resolution often result in a significant increase of the calculation time which make more difficult the repetition of numerical experiments, an important step to better understanding the global functioning of the area and its reaction to environmental forcings. A solution to avoid important calculation times is to use a dimensionless model. This type of model allows to conduct large amount of test in short amount of time. For instance, Lajaunie-Salla et al. (2021) used the dimensionless Eco3M-CarbOx model, which contains a carbonate module performing the resolution of the carbonate system based on total alkalinity (TA) and dissolved inorganic carbon (DIC). Even if the DIC, oceanic partial pressure of CO₂ ($p\text{CO}_2$) and total pH (pH_T) representations look reliable, Eco3m-CarbOx tends to minimize the range of TA variations during the year, resulting in a near constant TA (Lajaunie-Salla et al., 2021).

Here we try to provide a more realistic representation of carbonate system variables in the BoM. As a starting point, we used the concept of the dimensionless Eco3M-CarbOx model (Lajaunie-Salla et al., 2021), which aims to represent a small volume of surface water (i.e., 1 m³) in the BoM. We developed a planktonic ecosystem model which contains, among others, mixotrophic organisms, modified the carbonate module described by Lajaunie-Salla et al. (2021) and added it to our newly developed planktonic ecosystem model to obtain the Eco3M_MIX-CarbOx model (v1.0). We implemented two types of TA

formulation and compared the simulation results to in situ observations to identify which formulation was capable to deliver the more realistic results: (i) a formulation that only considers biological processes (referred to as autochthonous formulation) and (ii) a new TA formulation that depends only on salinity (referred to as allochthonous formulation).
80 Furthermore, we simulate air-sea CO₂ fluxes to determine whether the BoM act as a sink or a source of CO₂ and provide a detailed analysis of drivers of seawater pCO₂ variations for two specific hydrodynamic processes typical for the BoM: (i) Rhône River intrusion and (ii) summer upwelling events. With this study, we aim to provide a new tool which allow to obtain a reliable representation of the carbonate system in the simplest way as possible: by using a dimensionless
85 configuration which is easy to use, adapt and give results in a short amount of time.

Eco3M_MIX-CarbOx model contains both a mixotrophy compartment and a representation of the carbonate system. The model description is split in two parts: (i) a description of how the organisms and their dynamics are represented in the model, with a particular focus on mixotrophic organisms, and (ii) a more detailed description of the carbonate module and the associated dynamics. While (ii) is presented here, (i) has been presented in a companion paper (Barré et al., 2023a).

90 **2 Materials and methods**

2.1 Study area

The BoM is located in the NW Mediterranean Sea, in the eastern part of the Gulf of Lion near Marseille. Due to its proximity to Marseille, the second biggest city in France, and to other urbanized areas along the coast (e.g., Fos-sur-Mer and Berre Lagoon to the west), the BoM is strongly affected by anthropogenic forcings which results in significant inputs of
95 anthropogenic nutrients as ammonia and phosphate, chemical products, and organic matter (Millet et al., 2018) through urban rivers. Significant quantities of nutrients and freshwater are also provided by the Rhône River (Pont et al., 2002) of which the delta is located 35 km to the west of the bay. In specific wind conditions, Rhône River plume can be pushed eastwards, supplying the bay with nitrate which tend to boost the productivity of the area (Gatti et al., 2006; Fraysse et al., 2013, 2014). In addition to these inputs, the biogeochemical functioning of the BoM is affected by various hydrodynamic
100 processes including strong Mistral events (Yohia, 2017), upwelling events (Millot, 1990) which generally take place in specific locations: the Calanques of Marseille and the Côte Bleue, development of eddies (Schaeffer et al., 2011) and intrusions of oligotrophic water masses via the Northern Current (Barrier et al., 2016; Ross et al., 2016).

In Eco3M_MIX-CarbOx, environmental forcings are provided by in situ measurements of sea surface temperature (referred as temperature in the following), salinity and atmospheric pCO₂ in combination with simulation data of wind speed and solar
105 irradiance. Environmental forcings has already been described in detail in Barré et al. (2023a), their main characteristics are reminded in Table 1.

110 **Table 1. Data types and their sources used to drive the environmental forcing during the 2017 model run (based on Barré et al., 2023a).**

	Data type	Location	Time resolution
Sea surface temperature	Measurements	Planier station	Hourly
Salinity	Measurements	Carry buoy	Hourly
Wind	WRF model results	SOLEMIO station	Hourly
Irradiance	WRF model results	SOLEMIO station	Hourly
Atmospheric $p\text{CO}_2$	Measurements	Cinq Avenues station	Hourly

To evaluate our representation of carbonate system variables, we compared our model results to in situ measurements by using a carbonate parameters data set which includes TA, DIC, pH, $p\text{CO}_2$ and salinity data (<https://www.seaonoe.org>, last access: 14 February 2023). Measurements are performed fortnightly at SOLEMIO station.

115 A map of the study area showing the location of stations where measurements were carried, and places of interest can be found in Barré et al. (2023a).

2.2 Model description

In this study, we used the Eco3M_MIX-CarbOx model (v1.0) which was developed to represent the dynamics of the seawater carbonate system and mixotrophs in the BoM and was implemented using the Eco3M (Ecological Mechanistic and Molecular Modelling) platform (Baklouti et al., 2006a, b). Eco3M_MIX-CarbOx is a dimensionless model (0D): we
 120 consider a volume of 1 m^3 of surface water at SOLEMIO station, in this volume the state variables only vary over time as the model is not coupled with a hydrodynamic model. We chose to use a 0D configuration as this configuration has several advantages namely, calculation times are low (around 45 minutes in our case). It allows to make several test simulations to better understand the biogeochemical functioning of the BoM and its possible reactions to environmental forcings. In the following, we provide a detailed description of the carbonate system module. We also give a brief description of nutrients
 125 and organic matter representation. A detailed description of other compartments, especially of mixotrophs compartment can be found in Barré et al. (2023a). Equations and parameters used by the model are also explained in this previous study. The Eco3M_MIX-CarbOx model includes seven compartments: zooplankton, mixotrophs, phytoplankton, heterotrophic bacteria, labile dissolved organic matter, detritic particulate organic matter, and dissolved inorganic matter with the following carbonate system variables: dissolved inorganic carbon (DIC), total alkalinity (TA), pH calculated on total scale (pH_T), and
 130 oceanic partial pressure of CO_2 : ($p\text{CO}_2$). The carbonate system resolution required knowledge of at least two from among the four main variables of TA, DIC, pH_T and $p\text{CO}_2$. As TA and DIC are conserved, a requirement to solve the source-sinks state equations, we used those variables to perform the system resolution. To provide a more realistic representation of the carbonate system, we modified the carbonate module described by Lajaunie-Salla et al. (2021) by focusing mainly on the state equations of TA and DIC, as a realistic implementation of TA and DIC state variables is crucial to obtain reliable

135 estimates of the diagnostic variables pH_T , and pCO_2 . In addition to a modified carbonate module, Eco3M_MIX-CarbOx contains a mixotroph compartment which is crucial for a reliable representation of TA and DIC, as the presence of mixotrophs affects total photosynthesis, total respiration, as well as uptake and precipitation fluxes (Mitra et al., 2014).

2.2.1 Nutrients and organic matter

As we use a dimensionless configuration, we assume that nutrients are fully the result of autochthonous biological processes.

140 In other terms, we do not consider allochthonous inputs of nutrients (i.e., from rivers or atmosphere as instance). For all the simulations, nutrients dynamics are represented by the following state equations:

$$\begin{aligned} \frac{\partial NO_3}{\partial t} &= \text{Nitrif}_{NO_3}^{NH_4} - \sum_{i=1}^2 \left(\text{Upt}_{NO_3}^{PhyN_i} \right) - \text{Upt}_{NO_3}^{CMN_i} \\ \frac{\partial NH_4}{\partial t} &= \text{Excr}_{NH_4}^{COPN} + \text{Excr}_{NH_4}^{NCMN} + \text{Remin}_{NH_4}^{BACN} - \sum_{i=1}^2 \left(\text{Upt}_{NH_4}^{PhyN_i} \right) - \text{Upt}_{NH_4}^{CMN} - \text{Upt}_{NH_4}^{BACN} - \text{Nitrif}_{NH_4}^{NO_3} \\ \frac{\partial PO_4}{\partial t} &= \text{Excr}_{PO_4}^{COPP} + \text{Excr}_{PO_4}^{NCMP} + \text{Remin}_{PO_4}^{BACP} - \sum_{i=1}^2 \left(\text{Upt}_{PO_4}^{PhyP_i} \right) - \text{Upt}_{PO_4}^{CMP} - \text{Upt}_{PO_4}^{BACP} \end{aligned}$$

145 (1)

The NO_3^- concentration results from nitrification and phytoplankton and CM uptakes. NH_4^+ concentration results from copepods and NCM excretion, remineralisation by heterotrophic bacteria, heterotrophic bacteria, phytoplankton, and CM uptakes and losses from nitrification. PO_4^{3-} concentration results from copepods and NCM excretion, remineralisation by heterotrophic bacteria and heterotrophic bacteria, phytoplankton, and CM uptakes.

150 Such as nutrients dynamics, organic matter (OM, dissolved and particulate) dynamic is only the result of autochthonous biological processes (Eq. 2 and 3).

$$\begin{aligned} \frac{\partial DOC}{\partial t} &= \sum_{i=1}^2 \left(\text{Exu}_{DOC}^{PHYC_i} \right) + \sum_{i=1}^2 \left(\text{Exu}_{DOC}^{MIXC_i} \right) + \text{Excr}_{DOC}^{COPC} + \text{Mort}_{DOC}^{BACC} - \text{BP}_{DOC}^{BACC} \\ \frac{\partial DON}{\partial t} &= \sum_{i=1}^2 \left(\text{Exu}_{DON}^{PhyN_i} \right) + \sum_{i=1}^2 \left(\text{Exu}_{DON}^{MIXN_i} \right) + \text{Mort}_{DON}^{BACN} - \text{Upt}_{DON}^{CMN} - \text{Upt}_{DON}^{PICON} - \text{Upt}_{DON}^{BACN} \\ \frac{\partial DOP}{\partial t} &= \sum_{i=1}^2 \left(\text{Exu}_{DOP}^{PhyP_i} \right) + \sum_{i=1}^2 \left(\text{Exu}_{DOP}^{MIXP_i} \right) + \text{Mort}_{DOP}^{BACP} - \text{Upt}_{DOP}^{CMP} - \text{Upt}_{DOP}^{PICOP} - \text{Upt}_{DOP}^{BACP} \end{aligned}$$

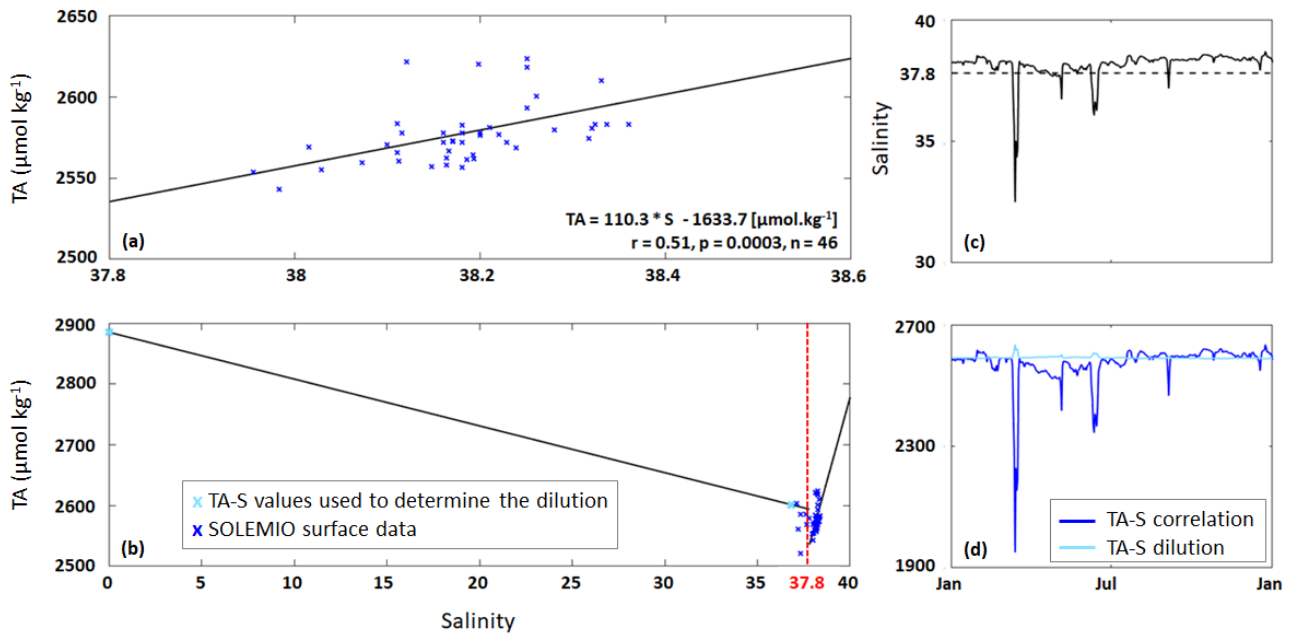
155 (2)

The concentration of dissolved organic (DOC), nitrogen (DON) and phosphorus (DOP) depends on phytoplankton and mixotrophs exudation, copepods excretion (DOC only), heterotrophic bacteria mortality (natural mortality) and CM, PICO and heterotrophic bacteria uptake.

$$\begin{aligned}
\frac{\partial \text{POC}}{\partial t} &= E_{\text{POC}}^{\text{COP}_C} + \text{Predation}_{\text{POC}}^{\text{COP}_C} - \text{BP}_{\text{POC}}^{\text{BAC}_C} \\
160 \quad \frac{\partial \text{PON}}{\partial t} &= E_{\text{PON}}^{\text{COP}_N} + \text{Predation}_{\text{PON}}^{\text{COP}_N} - \text{Upt}_{\text{PON}}^{\text{BAC}_N} \\
\frac{\partial \text{POP}}{\partial t} &= E_{\text{POP}}^{\text{COP}_P} + \text{Predation}_{\text{POP}}^{\text{COP}_P} - \text{Upt}_{\text{POP}}^{\text{BAC}_P}
\end{aligned}
\tag{3}$$

The concentration of particulate organic carbon (POC), nitrogen (PON), and phosphorus (POP) depends on copepods egestion, predation by higher trophic levels on copepods (closure terms of the model) and heterotrophic bacteria production and uptake. POM particles are large enough to sink, however, we do not consider a term to represent their removal from the surface box by sinking. In our case, the POM, such as the DOM and nutrients, stay in the box and is constantly recycling. A detailed description and formulations of processes can be found in Barré et al. (2023a). Processes notation description can be found in Table A1 (Appendix A).

2.2.2 TA formulation



170 **Figure 1.** (a) TA-S correlation (black line) based on SOLEMIO surface data excluding low salinities ≤ 37.8 (b) TA-S dilution (for $S \leq 37.8$) and TA-S correlation (for $S > 37.8$) (c) Salinity data used by the model (solid line) and $S = 37.8$ (dashed line) (d) TA calculated from TA-S correlation (Eq. 5) and TA-S dilution (Eq. 6).

In Eco3m-CarbOx, TA representation lack variations during the year. Eco3m-CarbOx did not account for TA inputs by rivers, especially by the Rhône River which has an average alkalinity of $2885 \mu\text{mol kg}^{-1}$ (Schneider et al., 2007). To remedy this shortcoming, we decided to express TA in two ways. In the first one, we considered only autochthonous TA variations.

In the second one, we considered allochthonous TA variations. We then compared the outputs from each formulation to in situ data to determine which formulation delivered the more realistic results.

For the autochthonous formulation, we relied on the Eco3M-CarbOx TA state equation which we modified to fit our modelled planktonic ecosystem. We first added a term of phosphate remineralisation by heterotrophic bacteria. By considering that the uptake of one mole of phosphate by phytoplankton increases TA by one mole, and vice versa, for one mole of phosphate released during remineralisation, TA decreases by one mole (Wolf-Gladrow et al., 2007a). As a last term we included the mixotrophic uptake of nutrients. TA is calculated as follows:

$$\frac{\partial TA}{\partial t} = 2 \cdot Diss_{TA}^{CaCO_3} + \sum_{i=1}^2 \left(Upt_{NO_3}^{PHY N_i} \right) + Upt_{NO_3}^{CMN} + \sum_{i=1}^2 \left(Upt_{PO_4}^{PHY P_i} \right) + Upt_{PO_4}^{CMP} + Remin_{NH_4}^{BACN} - \sum_{i=1}^2 \left(Upt_{NH_4}^{PHY N_i} \right) - Upt_{NH_4}^{CMN} - Remin_{PO_4}^{BACP} - 2 \cdot Prec_{TA}^{CaCO_3} - 2 \cdot Nitri_{TA}f_{TA}, \quad (4)$$

where i represents the number of organisms. Processes description can be found in Table A1 (Appendix A) and formulations are available in Barré et al. (2023a). In this formulation, TA only depends on biogeochemical processes (i.e., TA riverine inputs are excluded).

For the allochthonous formulation, we first determined an oceanic TA-S correlation (Eq. 5; Fig. 1a) using the measurements of carbonate system parameters at SOLEMIO station (see Sect. 2.1). We only considered the TA values associated to salinity values > 37.8 as 37.8 was used as a threshold value to identify low salinity events (LSE), associated to Rhone River plume intrusions in the BoM (Frayse et al 2014).

$$TA = 110.3 * S - 1633.7 \text{ (}\mu\text{mol kg}^{-1}\text{)} \quad (5)$$

Second, using only those TA values associated with LSE, we determined a separate TA-S formulation to quantify river water dilution (Eq. 6; Fig. 1b).

$$TA = -7.7 * S + 2885 \text{ (}\mu\text{mol kg}^{-1}\text{)} \quad (6)$$

The carbonate data set did not contain sufficient LSE data to create a reliable TA-S fit. Eq. (6) was therefore derived based on two TA-S data pairs: $TA = 2885.0 \mu\text{mol kg}^{-1}$ and $S = 0$, representative of water masses near Rhône River mouth (Schneider et al., 2007), and $TA = 2600.6 \mu\text{mol kg}^{-1}$ and $S = 36.82$, recorded at SOLEMIO station during a major LSE on March 15, 2017. Unlike Eq. (5), the TA-S dilution shows a negative slope typical of low salinity river water (Fig. 1b).

We implemented both TA-S formulations in our Eco3M_MIX-CarbOx model, and the formulation to be used was chosen based on the salinity : if salinity value used by the model for the time step considered ≤ 37.8 , the TA-S dilution (Eq.6) was

applied; else for salinity value > 37.8 the TA-S correlation was applied (Eq. 5, Fig. 1c,d). With this method, TA only depends on salinity (i.e., biological processes are neglected).

2.2.3 DIC formulation

210 The DIC formulation used in our Eco3M_MIX-CarbOx model is very similar to the formulation used in Eco3M-CarbOx except that we added the mixotroph organisms' processes to our equation. As a results, DIC depends on phytoplankton, mixotrophs, zooplankton and bacterial respiration, air-sea CO₂ fluxes (aeration process), dissolution of CaCO₃, phytoplankton and mixotrophs photosynthesis and precipitation of CaCO₃ (Eq.7).

$$\frac{\partial DIC}{\partial t} = \sum_{i=1}^2 \left(Resp_{DIC}^{PHYC_i} \right) + \sum_{i=1}^2 \left(Resp_{DIC}^{MIXC_i} \right) + Resp_{DIC}^{COPC} + BR_{DIC}^{BACC} + Diss_{DIC}^{CaCO_3} - \sum_{i=1}^2 \left(Photo_{DIC}^{PHYC_i} \right) - \sum_{i=1}^2 \left(Photo_{DIC}^{MIXC_i} \right) - Prec_{DIC}^{CaCO_3} - Aera_{DIC}$$

215 (7)

where *i* represents the number of organisms. Processes description can be found in Table A1 (Appendix A) and formulations are available in Barré et al. (2023a). As an additional modification, we use a more recent version of the gas transfer velocity calculation introduced by Wanninkhof (2014). The air-sea CO₂ fluxes are determined according to :

$$Aera = \frac{K_{ex}}{H} * \alpha * (pCO_{2,sw} - pCO_{2,atm})$$

220 (8)

where Aera is in mmol m⁻³ s⁻¹. K_{ex} represents the gas transfer velocity (Wanninkhof, 2014) in cm h⁻¹, α the CO₂ solubility coefficient (Weiss, 1974) in mol L⁻¹ atm⁻¹, pCO_{2,sw} the seawater pCO₂ modelled at the previous time step in μatm, pCO_{2,atm} the atmospheric pCO₂ from CAV in μatm and H the magnitude of the impacted layer in meters (in Eco3M_MIX-CarbOx, H = 1 m). K_{ex} is calculated using :

$$225 K_{ex} = 0.251 * U_{10}^2 * \left(\frac{660}{Sc} \right)^{\left(\frac{1}{2} \right)}$$

(9)

where U₁₀ is the wind speed in m s⁻¹ and Sc the Schmidt number calculated with the coefficients from Wanninkhof (2014). By convention, we will consider negative aeration values (i.e., pCO_{2,atm} > pCO_{2,sw}) to represent fluxes from the atmosphere into the ocean and vice versa. Furthermore, we will express air-sea CO₂ fluxes in the more frequently used units of mmol m⁻² per unit time.

230

Figure 2 illustrates the concept of 0D and summarizes hypotheses used in this study with Eco3M_MIX-CarbOx.

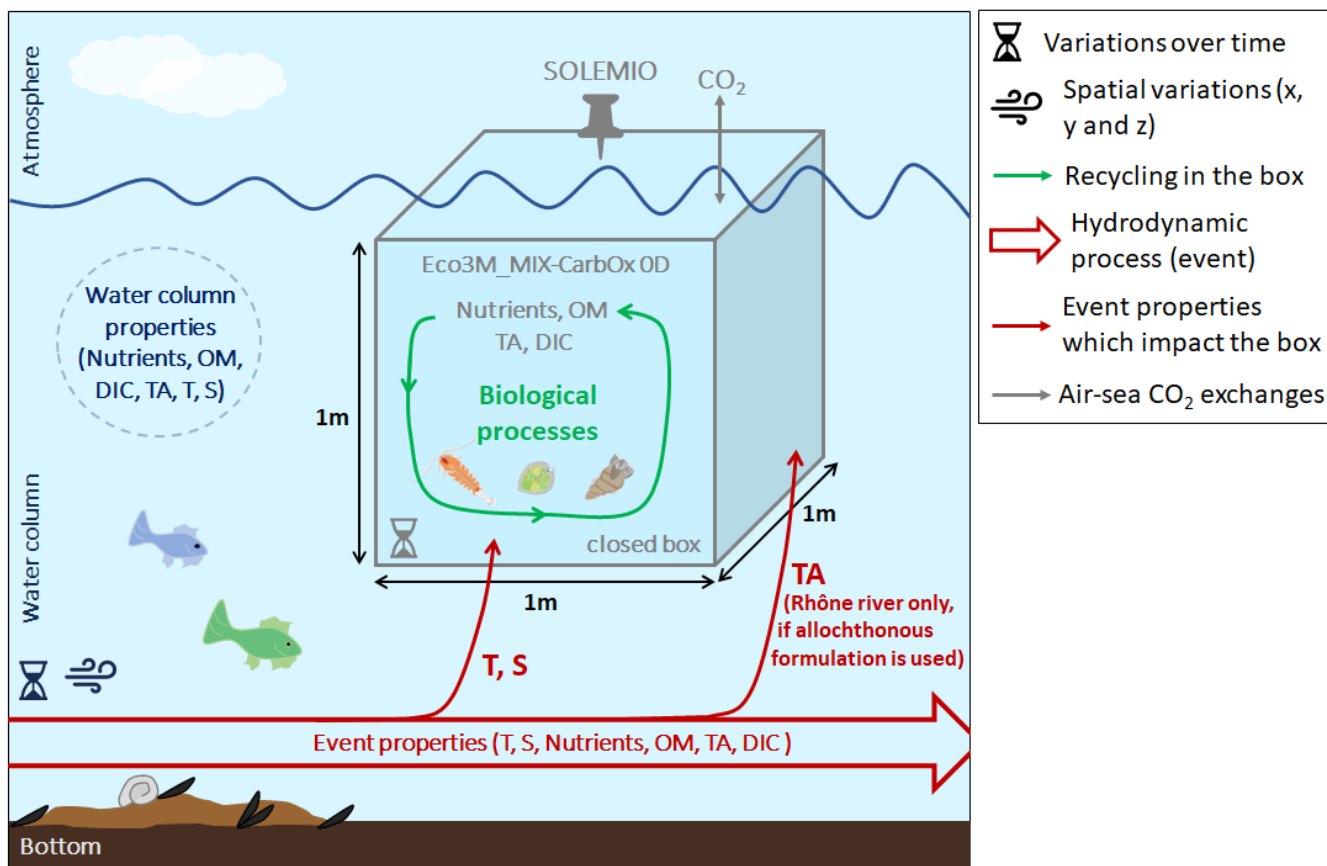


Figure 2. Schematic representation of 0D concept and summary of hypotheses used in this study with Eco3M_MIX-CarbOx. T: temperature, S: Salinity and OM: Organic matter.

235 2.2.4 pH_T and pCO_2 calculation

Solving the equations of the carbonate system requires knowledge of TA and DIC. Depending on the TA formulation used, the steps followed by the model to issue the new pH_T and pCO_2 are described on Fig. 3.

If TA is calculated using the Eq. (4), biogeochemical and aeration processes are applied as described in Eqs. (4) and (7) in order to deliver new ([t] time step) TA and DIC : Air-sea CO₂ fluxes are calculated from temperature, salinity, wind speed, atmospheric pCO_2 and seawater pCO_2 , and biogeochemical processes required, at least, temperature to be computed and
 240 atmospheric pCO_2 and seawater pCO_2 , and biogeochemical processes required, at least, temperature to be computed and solar irradiance. When calculated, processes are applied in the form of fluxes to the previous TA and DIC ([t-1] time step values) to solve their respective state equation. The pH_T and pCO_2 calculation is, then, performed using in addition to TA and DIC, temperature and salinity data. pH_T is calculating using a buffering value (B) defined as the pH variation induced by an addition of acid or base to a specific solution (Van Slycke, 1922). In seawater, B can be expressed in terms of TA
 245 (Middelburg, 2019) which yields:

$$B = \frac{\partial TA}{\partial pH_T} \Leftrightarrow \Delta pH_T = \frac{\partial TA}{\sum_{i=1}^n B_i} \quad (10)$$

where i represents a chemical species contributing to TA. pCO_2 is obtained using:

$$pCO_2 = \frac{DIC * [H^+]^2}{[H^+]^2 + K_1 * [H^+] + K_1 * K_2} * \frac{10^6}{K_0 * FugFac} \quad (11)$$

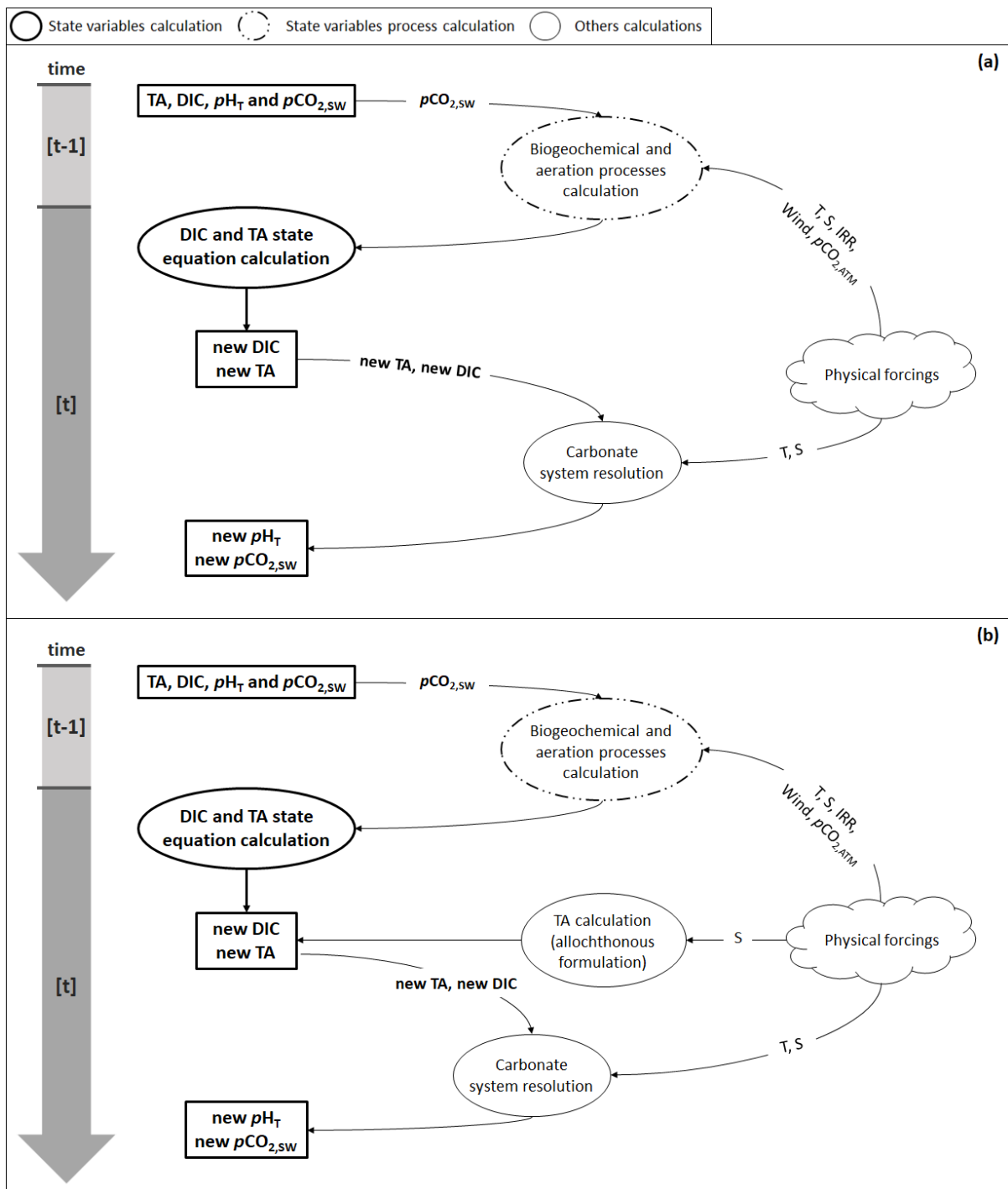
where pCO_2 is in μatm and FugFac represents the fugacity factor. A more detailed description of the calculation is provided in Appendix B. At the end of the time step, TA, DIC, pH_T and pCO_2 are written to file (Fig. 3a).

When TA is calculated using Eqs. (5) and (6), the biogeochemical and aeration fluxes computed during the first stage are only applied to DIC from the preceding time step, while TA is calculated after DIC based on the salinity data from the current time step. All subsequent steps are unchanged (Fig. 3b).

Simulations were conducted using both formulations (autochthonous and allochthonous) for the year 2017 (Table 2, SIMC0 and SIMC1).

Table 2. Summary of simulation properties.

Simulation name	Total Alkalinity	Temperature	Salinity	Air-sea CO ₂ fluxes	Biology
SIMC0-Modelled TA (autochthonous formulation)	Modelled	Temperature file	Salinity file	Allowed	Yes
SIMC1-Calculated TA (allochthonous formulation)	Calculated: TA = f(S)	Temperature file	Salinity file	Allowed	Yes
SIMC2-Aeration effect	Calculated: TA = f(S)	Temperature file	Salinity file	Not allowed	Yes
SIMC3-Biology effect	Calculated: TA = f(S)	Temperature file	Salinity file	Not allowed	No
SIMC4-Solubility effect	Calculated: TA = f(S)	Constant: T = 16.4°C	Constant: S = 38.1	Not allowed	No



260 **Figure 3.** Flow diagram illustrating the steps needed to calculate pH_T and pCO_2 (a) using the autochthonous formulation (Eq. 4) and (b) with the allochthonous formulation (Eq. 5 and 6). Physical forcings include temperature (T), salinity (S), solar irradiance (IRR), wind speed (Wind) and atmospheric pCO_2 ($pCO_{2,ATM}$).

2.3 $p\text{CO}_2$ decomposition

265 To determine the drivers of temporal variability of $p\text{CO}_2$, we use two types of $p\text{CO}_2$ decomposition. The first is based on Lovenduski et al. (2007) and evaluates TA, DIC, temperature, and salinity contributions to $p\text{CO}_2$ variations, while the second is based on Turi et al. (2014) and consider the contributions of biology, air-sea CO_2 fluxes and solubility.

2.3.1 TA, DIC, T, and S drivers

270 Following the reasoning presented in Lovenduski et al. (2007), $p\text{CO}_2$ variations can be expressed as the sum of variations generated by changes in TA, DIC, temperature and salinity as follow:

$$\begin{aligned} \Delta p\text{CO}_2 &= \Delta p\text{CO}_2^{TA} + \Delta p\text{CO}_2^{DIC} + \Delta p\text{CO}_2^T + \Delta p\text{CO}_2^S \\ \Delta p\text{CO}_2 &= \frac{\partial p\text{CO}_2}{\partial \text{TA}} * (\text{TA} - \overline{\text{TA}}) + \frac{\partial p\text{CO}_2}{\partial \text{DIC}} * (\text{DIC} - \overline{\text{DIC}}) + \frac{\partial p\text{CO}_2}{\partial T} * (T - \overline{T}) + \frac{\partial p\text{CO}_2}{\partial S} * (S - \overline{S}), \end{aligned} \quad (12)$$

275 where $\Delta p\text{CO}_2$ is in μatm . The overbar in $\overline{\text{TA}}$, $\overline{\text{DIC}}$, \overline{T} and \overline{S} denotes the annual mean. Freshwater inputs can induce changes in TA and DIC. Though, we isolate the changes of TA and DIC due to variations in freshwater inputs using the salinity-normalised TA (nTA) and DIC (nDIC)) which are obtained by dividing the considered variable by in situ salinity and by multiplying the result by mean in situ salinity and adding another term to regroup them. For simplicity, we only use one term to designate salinity and freshwater inputs. Eq. (12) can thus be rewritten as:

$$\begin{aligned} \Delta p\text{CO}_2 &= \Delta p\text{CO}_2^{nTA} + \Delta p\text{CO}_2^{nDIC} + \Delta p\text{CO}_2^T + \Delta p\text{CO}_2^{S+FW} \\ 280 \Delta p\text{CO}_2 &= rS * \frac{\partial p\text{CO}_2}{\partial \text{TA}} * (\text{TA} - \overline{\text{TA}}) + rS * \frac{\partial p\text{CO}_2}{\partial \text{DIC}} * (\text{DIC} - \overline{\text{DIC}}) + \frac{\partial p\text{CO}_2}{\partial T} * (T - \overline{T}) + \frac{\partial p\text{CO}_2}{\partial S} * (S - \overline{S}) + rS_{TA} * \frac{\partial p\text{CO}_2}{\partial \text{TA}} \\ &* (S - \overline{S}) + rS_{DIC} * \frac{\partial p\text{CO}_2}{\partial \text{DIC}} * (S - \overline{S}), \end{aligned} \quad (13)$$

285 where rS represents the ratio of salinity to mean salinity, rS_{TA} the ratio of nTA to salinity and rS_{DIC} the ratio of nDIC to salinity. See Appendix A in Lovenduski et al., (2007) for more details about the computation. Derivatives are obtained using the approach suggested by Sarmiento and Gruber, (2006).

2.3.2 Contributing processes

The second decomposition (Turi et al., 2014) aims to estimate the contribution of air-sea CO_2 exchanges, biological processes, and solubility effects to $p\text{CO}_2$ variations:

$$\Delta p\text{CO}_2 = \Delta p\text{CO}_2^{Aeration} + \Delta p\text{CO}_2^{Biology} + \Delta p\text{CO}_2^{Solubility}$$

With the modelling approach used here, we can easily identify the individual processes and evaluate their effect on $p\text{CO}_2$ variations. Several simulations are required to identify and separate the effects of the underlying processes (see Table 2, SIMC2 to SIMC4). SIMC2 aimed to quantify the effect of aeration process on $p\text{CO}_2$ variations. Starting from SIMC1, we disabled the air-sea CO_2 exchanges. SIMC3 aimed to estimate the effects of biology. Using the above reasoning, we deactivated all biological processes, i.e., neither the biology nor aeration was activated in SIMC3. Finally, SIMC4 aimed to evaluate the effect of solubility on $p\text{CO}_2$ variations. This was achieved by keeping both temperature and salinity constant, using their annual means. The three terms of the Eq. (14) can be calculated as follow:

$$\Delta p\text{CO}_2^{\text{process}_i} = p\text{CO}_2^{\text{SIMC}(i-1)} - p\text{CO}_2^{\text{SIMC}(i)}, \quad (15)$$

where i is the simulation number for the process considered ($2 \leq i \leq 4$). The order in which the simulations are run is particularly important. For instance, we quantified the aeration effect (by deactivating aeration) before examining the effect of biological processes (also by deactivating them) because of the impact the biology can have on seawater $p\text{CO}_2$ and on aeration fluxes. Using similar reasoning, the impact of the biology is assessed before the impact of solubility (obtained by setting temperature and salinity constant) temperature itself has a significant effect on the biology (Lajaunie-Salla et al., 2021).

2.4 Statistical indicators

We used four statistical indicators for the comparison between simulation and SOLEMIO data: the percentage bias (%BIAS), the average error (AE), the average absolute error (AAE) and the root mean square deviation (RMSD, also refer as root mean square error in the literature - RMSE). They were used with two Eco3M_MIX-CarbOx simulations (SIMC0 and SIMC1) and the reference Eco3M-CarbOx simulation (Lajaunie-Salla et al., 2021). The %BIAS is calculated as follow:

$$\% \text{BIAS} = \frac{\sum_{i=1}^N (O_i - M_i)}{\sum_{i=1}^N O_i} * 100 \quad (16)$$

where O represents the observations and M the model results (Allen et al., 2007). This indicator allows to quantify the model's tendency to under- or overestimate the observations. The closer the value is to 0, the better the model. Here, a positive %BIAS means that the model underestimated the in situ observations and vice versa. On an indicative basis, the %BIAS can be interpreted according to Marechal (2004): Absolute values of %BIAS allow to assess the overall agreement between the model results and observations and the agreement is considered: excellent if $\% \text{BIAS} < 10 \%$, very good if $10 \% \leq \% \text{BIAS} < 20 \%$, good if $20 \% \leq \% \text{BIAS} < 40 \%$ and poor otherwise.

We based our calculation of AE, AAE and RMSD on Stow et al. (2009). Together, these three statistical indicators provide
320 an indication of model prediction accuracy.

$$AE = \frac{\sum_{i=1}^N (O_i - M_i)}{n} \quad (17)$$

$$AAE = \frac{\sum_{i=1}^N (|O_i - M_i|)}{n} \quad (18)$$

$$325 \quad RMSD = \sqrt{\frac{\sum_{i=1}^N (O_i - M_i)^2}{N}} \quad (19)$$

The three of them aim to measure the size of the discrepancies between model results and observations, the closer the value
is to 0, the better the agreement between model results and observations. However, when interpreting AE, it is important to
note that value near zero can be misleading because negative and positive discrepancies can cancel each other. That is why it
330 is important to calculate, in addition to AE, AAE and RMSD which allow to overcome this effect (Stow et al., 2009). Such
as %BIAS, a positive value of AE means that the model underestimated the in situ observations and vice versa.

The model data is averaged using the mean of the output from the date in question \pm five days. Using temporal mean and
standard deviation of model results allowed us to better account of variability at SOLEMIO station. By comparing the
statistical indicators obtained for SIMC0, SIMC1 and Eco3M-CarbOx we also obtained an indication of how changes in the
335 carbonate formulation affected the results.

3 Results

3.1 Carbonate system variables

We performed an initial qualitative evaluation of Eco3M_MIX-CarbOx, comparing the output of SIMC0 (using the
autochthonous TA formulation) and SIMC1 (using allochthonous TA formulation) for TA, DIC, pCO_2 and pH_T to the
340 corresponding SOLEMIO surface data for 2017 (Figs. 4a-d). The different TA formulations yielded very different model
outputs for DIC, pCO_2 and pH_T (Figs. 4f-h).

TA observations varied between 2560.8 and 2623.9 $\mu\text{mol kg}^{-1}$, with no apparent seasonal pattern (Fig. 4a). This variability is
successfully represented by SIMC1, but not SIMC0 (SIMC1 range: 2540 to 2635 $\mu\text{mol kg}^{-1}$). SIMC0 produces TA values
that show a gradual and near-linear decrease from 2578 $\mu\text{mol kg}^{-1}$ in early January to 2572 $\mu\text{mol kg}^{-1}$ at the end of the year.
345 The differences between SIMC0 and SIMC1 are most pronounced between August and December where SIMC1 delivers
systematically higher TA values compared to SIMC0 (Fig. 4e).

With regard to DIC, both SIMC0 and SIMC1 are capable of reproducing the seasonal variability present in the in situ data. From November to April, DIC has higher values (around $2320 \mu\text{mol kg}^{-1}$ in both simulations), with lower values during the rest of the year (both have a minimum August, SIMC0: $2234 \mu\text{mol kg}^{-1}$ and SIMC1: $2254 \mu\text{mol kg}^{-1}$; Fig. 4b). At the beginning of the year, SIMC1 seems to be closer to the observations than SIMC0 which shows fewer variations (e.g., SIMC1 appears to be better at reproducing the decrease visible at the end of April). Differences between SIMC0 and SIMC1 for DIC are similar to those observed for TA (Fig. 4e,f) although in absolute terms, they are only about half of what we observed for TA. Nevertheless, these results show that the choice of the TA formulation strongly affects the DIC model results (Fig. 4f). The in situ $p\text{CO}_2$ data exhibits strong variations throughout the year, especially from May to November which are well represented in both simulations (Fig. 4c). Between January and April, both simulations overestimate the in situ $p\text{CO}_2$ values: while the simulations both predict $p\text{CO}_2$ values close to the CAV atmospheric $p\text{CO}_2$ of about $415 \mu\text{atm}$, $p\text{CO}_2$ observed at SOLEMIO is lower indicating under-saturation. For both simulations a strong decrease of $p\text{CO}_2$ is modelled on March 15th, in response to a Rhône River intrusion in the BoM. This event is particularly marked in the SIMC1 model results which show a decrease from 450 to $300 \mu\text{atm}$ (compared to a decrease from 415 to $358 \mu\text{atm}$ with SIMC0). While this decrease is also visible in the in situ data it is more moderate (392 to $367 \mu\text{atm}$).

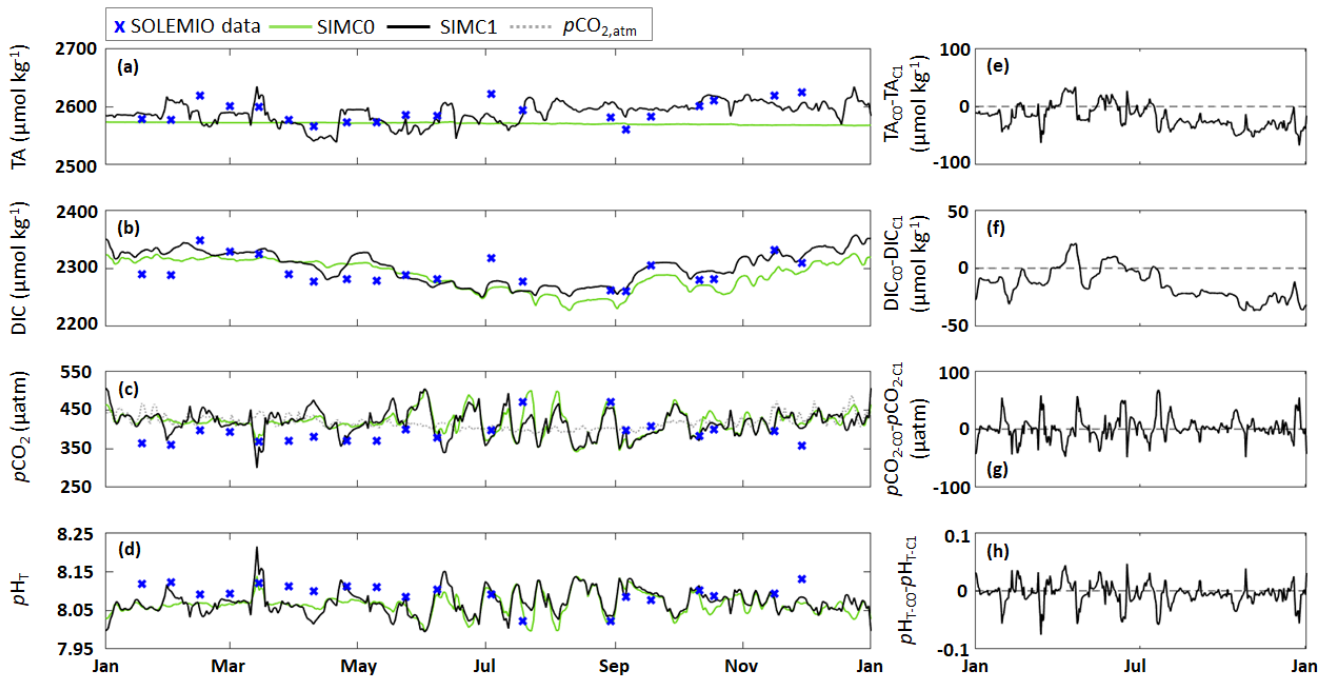


Figure 4. (a-d) Comparison of model outputs from the SIMC0 (autochthonous formulation) and SIMC1 (allochthonous formulation), model runs showing daily averages of (a) TA, (b) DIC, (c) seawater $p\text{CO}_2$ and CAV atmospheric $p\text{CO}_2$ and (d) pH_T . (e-h) Differences between SIMC0 and SIMC1 outputs for each variable (VARC0 – VARC1).

Regarding pH_T , both simulations produced similar dynamics as for $p\text{CO}_2$ (Figs. 4d vs 4c). Both simulations deliver good representations of the observed pH_T variations between May and November while from January to April both simulations

underestimate the in situ (in situ: 8.12 vs simulations: 8.07). The Rhône River intrusion is also visible in the pH_T data which exhibits a sudden increase. While both simulations show this increase, it is more pronounced in the SIMC1 results (increase from 8.04 to 8.21) compared to SIMC0 (8.07 to 8.14), but in both cases larger than in the observations (8.09 to 8.12).

370 The differences between both simulations for $p\text{CO}_2$ and pH_T do not exhibit any noticeable trend (Fig. 4g,h). However, looking at the annual average, SIMC1 produces lower (higher) $p\text{CO}_2$ (pH_T) values compared to SIMC0 with a mean difference of $2.3 \mu\text{atm}$ (-5×10^{-3}). Moreover, for both variables, the differences between SIMC0 and SIMC1 are more pronounced at the beginning of the year.

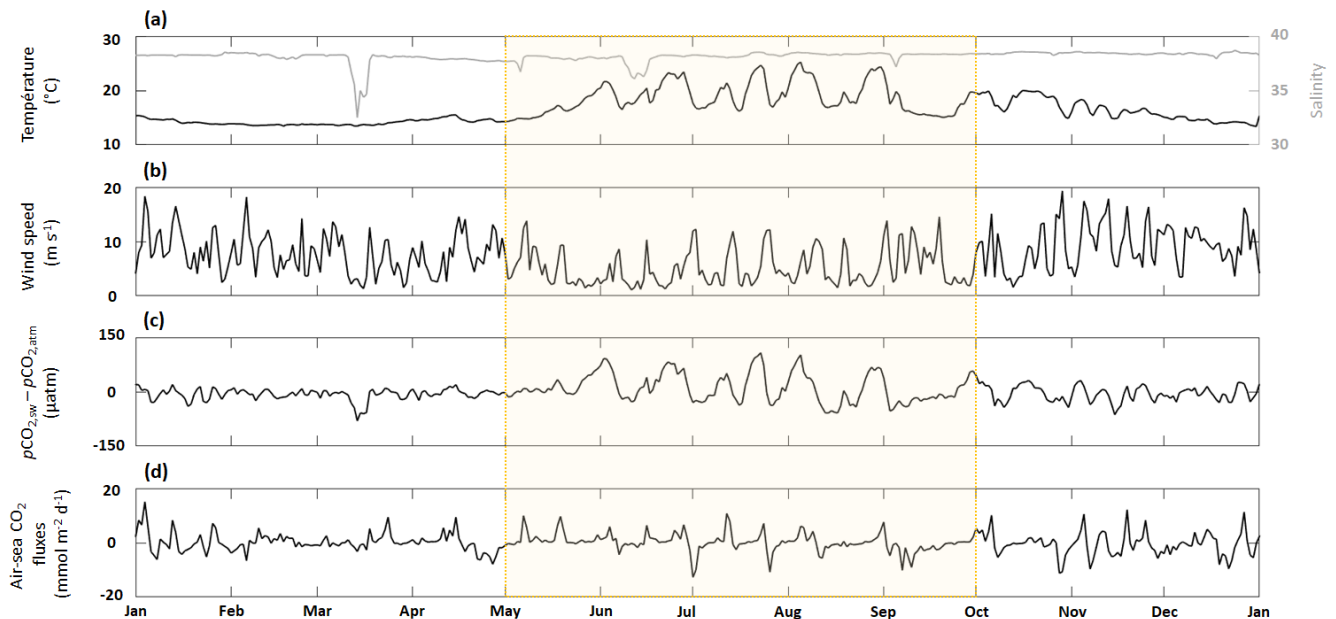
For statistical indicators, %BIAS values are systematically lower than 10 %, with the highest values obtained for $p\text{CO}_2$ with
 375 ~ 6 % while the remaining variables had values < 1 %. Similarly, $p\text{CO}_2$ had the highest RMSD, AAE and AE which suggests that this parameter is not as well represented in the model as the other variables. Furthermore, SIMC1 produced the best TA representation resulting in the lowest values for %BIAS, AE, AAE and RMSD (Table 3). Moreover, SIMC1 produced an annual mean-TA that was closest to the observations. While the SIMC0 and Eco3m-CarbOx results are fairly similar. SIMC0 produced a slightly better representation of TA compared to Eco3m-CarbOx (%BIAS, AE, AAE and RMSD slightly
 380 lower). For pH_T , SIMC1 outperformed SIMC0 based on %BIAS (Table 3), however, AE, AAE and RMSD values are similar for the three simulations. We then performed the calculation of statistical indicators on H^+ concentration as, according to some authors (Kwiatkowski & Orr, 2018), comparing H^+ concentrations is a better practice than comparing pH. Results are available in Appendix C. Based on Table C1, SIMC1 also outperformed SIMC0 based on AE and AAE. For
 385 studying DIC and $p\text{CO}_2$, the situation is less clear as the simulations performed differently for different indicators, making it difficult to pick a clear winner. Still SIMC1 shows the best AAE and RMSD values for DIC, and the best %BIAS, AE, and AAE for $p\text{CO}_2$. In conclusion, SIMC1 shows the best overall indicator values for the examined variables (more specifically, it outperformed the other simulations in 13 of 20 indicator comparisons when including H^+ concentrations comparison).

390 **Table 3. Comparing the different model results to surface observations at SOLEMIO station for TA, DIC, seawater $p\text{CO}_2$, and pH_T . N represents the number of observations. Mean, SD, AE, AAE and RMSD are in the same unit than the considered variable, i.e.: $\mu\text{mol kg}^{-1}$ for TA and DIC and μatm for $p\text{CO}_2$. % BIAS is without unit.**

		TA	DIC	$p\text{CO}_2$	pH_T
N	Observations	20	20	20	20
Mean \pm SD	Observations	2591.2 ± 19.4	2294.9 ± 24.0	391.0 ± 31.0	8.09 ± 0.030
	SIMC0	2576.1 ± 1.5	2293.6 ± 25.1	413.5 ± 16.5	8.07 ± 0.015
	SIMC1	2588.6 ± 16.4	2301.1 ± 24.5	409.1 ± 21.4	8.07 ± 0.020
%BIAS	CarbOx	2574.5 ± 3.6	2292.5 ± 26.0	413.9 ± 15.9	8.07 ± 0.010
	SIMC0	0.58	0.05	-5.75	0.29
	SIMC1	0.09	-0.27	-4.61	0.21
	CarbOx	0.64	0.1	-5.86	0.29

AE	SIMC0	15.12	1.25	-22.5	0.02
	SIMC1	2.57	-6.2	-18.02	0.02
	CarbOx	16.7	2.4	-22.9	0.02
AAE	SIMC0	18.7	20.4	35.9	0.03
	SIMC1	16.3	17.2	34.7	0.03
	CarbOx	20.1	21.2	35.3	0.03
RMSD	SIMC0	24.90	24.26	38.75	0.04
	SIMC1	20.03	21.83	40.27	0.04
	CarbOx	26.56	24.90	38.29	0.04

3.2 Air-sea CO₂ fluxes



395 **Figure 5.** Time series of (a, e) in situ daily average sea surface temperature (black line) and salinity (grey line) (b, f) SIMC1 daily average wind speed (c, g) the difference between SIMC1 daily average seawater $p\text{CO}_2$ and in situ daily average atmospheric $p\text{CO}_2$ (d, h) SIMC1 daily average air-sea CO₂ fluxes (aeration process). The summer upwelling period (from 1 May to 1 October) is highlighted in yellow.

Throughout 2017 temperature varied from 13.3 to 25.9 °C (Fig. 5a) with the highest variability visible during the summer upwelling period (SUP). Apart from four low salinity events in March, May, June, and September (all corresponding to the Rhône River intrusions) the salinity remained close to its mean value of 38.1 (Fig. 5a).

400 Wind speed was highly variable with several strong gusts, especially during winter when wind speeds often exceeded 10 m s^{-1} (Fig. 5b). Wind speed tends to be lower during summer and SUP, although these periods also show numerous strong wind events ($> 10 \text{ m s}^{-1}$).

The sea-air $p\text{CO}_2$ difference exhibits the same seasonality as temperature, with high positive values during summer while oscillating about zero during the rest of the year. In general, the sea-air $p\text{CO}_2$ difference combines the patterns from
405 temperature, salinity and wind speed which are the main underlying forcings. The local minimum in March, corresponds to an extremely low salinity event (Fig. 5c). However, during the SUP the sea-air $p\text{CO}_2$ difference is mostly driven by temperature as seen by the high variability between May and October which coincide with the largest temperature variations. In contrast, air-sea CO_2 fluxes do not show any seasonality, with values oscillating about zero throughout the year (Fig. 5d) yielding an integrated total of $-0.21 \text{ mmol m}^{-2}$ per year. Maximum positive values are obtained from November to March
410 when wind speeds are highest. Extreme negative value (-13 mmol m^{-2} per day) can be seen in July coinciding with high wind speed, negative sea-air $p\text{CO}_2$ difference and a significant drop in temperature.

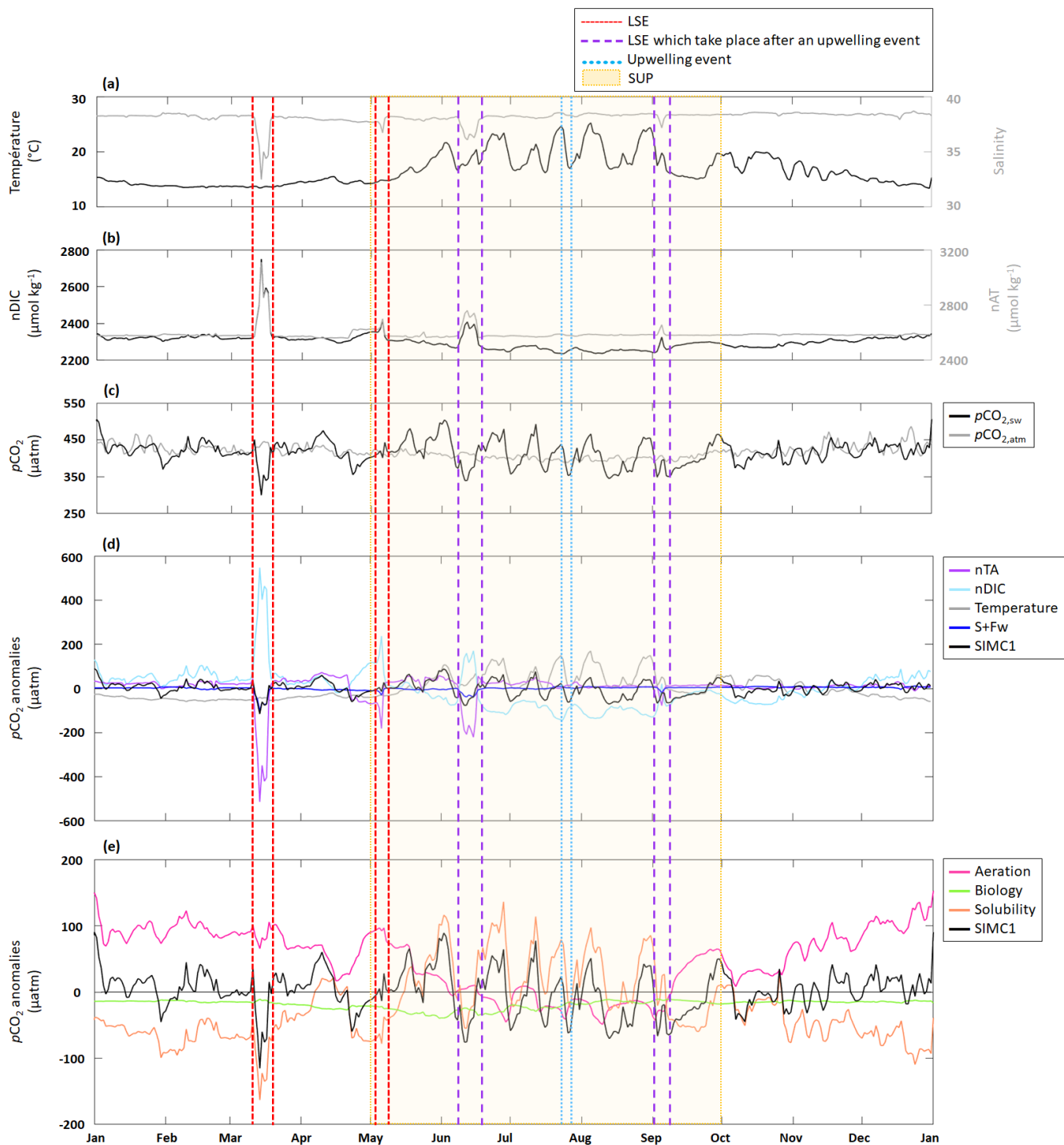
3.3 Main drivers of $p\text{CO}_2$ dynamics

3.3.1 Annual scale

Following the approach from Lovenduski et al. (2007), we used temperature (Fig. 6a), as well as salinity (S), freshwater
415 inputs (Fw), nTA and nDIC (Fig. 6b) contributions to identify the underlying dynamics in the observed $p\text{CO}_2$ variations (Fig. 6c). Seasonal variations in temperature (Fig. 6a) produce seasonal anomalies in $p\text{CO}_2$ with negative anomalies dominating from November to May and mostly positive anomalies throughout the remainder of the year (Fig. 6d). Anomalies generated by S+Fw do not exhibit any seasonality but remain close to zero throughout the year, unless there is an LSE, during which the anomalies turn negative ($-101 \mu\text{atm}$, $-30 \mu\text{atm}$, $-40 \mu\text{atm}$ and $-20 \mu\text{atm}$ for the four LSE). Anomalies generated by nDIC
420 show the opposite seasonal trend compared to the anomalies generated by temperature, i.e., from November to May the nDIC-generated anomalies are positive and negative during the rest of the year. The four LSE are also clearly visible in the nDIC-generated anomalies which exhibit sharp increases (increase of $506 \mu\text{atm}$, $253 \mu\text{atm}$, $243 \mu\text{atm}$ and $152 \mu\text{atm}$ respectively). Also, nTA does not produce any seasonality in the anomalies but exhibits sharp decrease during the four LSE (decrease of $548 \mu\text{atm}$, $242 \mu\text{atm}$, $239 \mu\text{atm}$ and $90 \mu\text{atm}$ respectively).

425 Following the approach by Turi et al. (2014), we examined the effects of aeration, biological processes, and solubility on $p\text{CO}_2$ variability (Fig. 6e). Aeration produced anomalies very similar to those observed for nDIC (Fig. 6d): positive from November to May and negative during the rest of the year. Since CO_2 solubility is controlled by temperature and salinity, solubility-generated anomalies essentially follow the trends and seasonality seen in temperature and S+Fw-generated anomalies (Fig. 6d): negative from November to May and mostly positive during the rest of the year (mean of $+9.2 \mu\text{atm}$).
430 The four LSE are also visible in the solubility-generated anomalies generating strong decreases (Fig. 6e). However, only two LSE are easily identifiable (15 March with a drop from $-41 \mu\text{atm}$ to $-163 \mu\text{atm}$ and 6 May with a drop from $8 \mu\text{atm}$ to -75

435 μatm) while the other two appear to be obscured by temperature-related counter-movements. Since aeration- and solubility-generated anomalies show opposite seasonality, they partly cancel each other out. While aeration seems to dominate from November to May, (apart from LSE), solubility appears to dominate from May to November and during LSE. Biological processes are never the dominant driver of $p\text{CO}_2$ variations as they are systematically smaller (by a factor of 2 to 3) than aeration and solubility-generated anomalies (Fig. 6e). Biology-induced anomalies are always negative, providing evidence that biological processes always decrease $p\text{CO}_2$.



440 **Figure 6.** Time series for 2017 of daily average (a) in situ temperature and salinity (b) modelled nDIC and nTA (c) modelled seawater and in situ atmospheric $p\text{CO}_2$ (d) $p\text{CO}_2$ anomalies generated by DIC, TA, Fw+S and temperature based on the approach in Lovenduski et al. (2007) (Note: the dark blue line is sometimes obscured by the black line, especially in March. An enlargement

of the panel d is available in Appendix D) (e, j) $p\text{CO}_2$ anomalies generated by aeration, solubility, and biological processes based on the approach in Turi et al. (2014). LSE and an upwelling event have been highlighted. The summer upwelling period (SUP) is indicated by yellow shading.

3.3.2 During the summer upwelling period (SUP)

The SUP is characterized by significant temperature variations (Fig. 6a) due to periodic upwelling events. During the 2017 SUP, there were three LSE which will be excluded here as we discuss them in the following section. $n\text{TA}$ is nearly constant during the SUP while $n\text{DIC}$ shows marked variations (Fig. 6b) that are directly linked to variations in DIC (see Section 3.1). $p\text{CO}_2$ is also highly variable during the SUP (Fig. 6c). Using the approach from Lovenduski et al. (2007) (Fig. 6d), the SUP is characterized by a strong contribution of temperature which shows strong positive anomalies (maximum of 170 μatm reached on 5 August), and $n\text{DIC}$ which shows strong negative anomalies (minimum of -142 μatm reached on 24 July). $S+\text{Fw}$ and $n\text{TA}$ do not represent significant drivers with anomalies remaining close to zero. Using the approach in Turi et al. (2014) (Fig. 6e), we can see that solubility is a major driver producing large amplitude variations in the $p\text{CO}_2$ anomalies connected to similar variations in temperature (a drop in temperature causes the anomaly to change from positive to negative and vice versa) (Fig. 6a). Aeration, which mostly generates negative anomalies, counteracts solubility. During the SUP, we also observed an increase of biological processes contribution since associated anomalies further decrease at the beginning of the period (from -22 μatm on 1 May to -40 μatm on 31 May).

Focusing on the upwelling event that took place between 23-27 July, we observe a sharp decrease in temperature (from 24.6 $^{\circ}\text{C}$ to 16.9 $^{\circ}\text{C}$; Fig. 6a), no variation in $n\text{TA}$, and a slight increase in $n\text{DIC}$ (from 2242 $\mu\text{mol kg}^{-1}$ to 2269 $\mu\text{mol kg}^{-1}$; Fig. 6b). The event is also associated with a strong $p\text{CO}_2$ decrease (from 438 μatm to 353 μatm ; Fig. 6c). Using the approach in Lovenduski et al., (2007) we observed a decrease of the temperature-generated anomaly (from 148 μatm at the beginning of the event to 5 μatm at the peak of the event). At the same time, the $n\text{DIC}$ -generated anomaly become less negative (from -142 μatm at the beginning of the event to -79 μatm at the peak of the event). Neither $n\text{TA}$ nor $S+\text{Fw}$ seem to have any significant impact on $p\text{CO}_2$ anomalies. Using the approach in Turi et al. (2014) (Fig. 6e), the upwelling event is characterized by decrease of solubility-generated anomalies (from 79 μatm at the beginning of the event to -24 μatm at the end of the event). Anomalies generated by aeration and biological processes tend to respectively become positive and less negative at the end of the event (aeration: -45 μatm to 3 μatm ; biological processes: -30 μatm to -20 μatm).

3.3.3 During a low salinity event (LSE)

There were four LSE during 2017: on 15 March, 6 May, 15 June, and 5 September. All four LSE show similar patterns, namely strong decrease in salinity (Fig. 6a) which in turn leads to an increase in both $n\text{TA}$ and $n\text{DIC}$ (Fig. 6, Table 4). Apart from the 5 September LSE which shows an increase in $p\text{CO}_2$, the remaining LSE coincide with significant $p\text{CO}_2$ decreases (Fig. 6c, Table 4).

475

Table 4. Change in S, nTA, nDIC and $p\text{CO}_2$ from before to during a LSE.

	S	nTA ($\mu\text{mol kg}^{-1}$)	nDIC ($\mu\text{mol kg}^{-1}$)	$p\text{CO}_2$ (μatm)
15 March	38.3 to 32.5	2570 to 3110	2320 to 2750	450 to 300
6 May	37.8 to 36.7	2560 to 2700	2308 to 2420	420 to 401
15 June	38.1 to 36.0	2580 to 2760	2273 to 2409	504 to 340
5 September	38.3 to 37.1	2583 to 2658	2241 to 2327	348 to 396

When using Lovenduski et al., (2007) approach, LSE that do not take place immediately after an upwelling event (i.e., 15 March and 6 May) exhibit similar combinations of driver contributions, e.g., nTA and S+Fw create strong negative anomalies in both LSE (with combined (nTA+S+Fw) contributions of: -614 μatm on 15 March and -211 μatm on 6 May), which are partially cancelled out by nDIC opposite contribution (547 μatm on 15 March and 235 μatm on 6 May). While temperature-generated anomalies showed no change during either event, it is still negative and by adding its effect to those obtained for nTA and S+Fw, we obtain a combined effect of -656 μatm on 15 March and -241 μatm on 6 May.

LSE that take place immediately after a summer upwelling event (i.e., 15 June and 5 September), show similar variations of salinity, nTA, nDIC and $p\text{CO}_2$ but also show an increase of temperature (from 16.5 °C to 20.5 °C on 15 June and 17.5 °C to 19.8 °C on 5 September; Fig. 6a). Also, the factors driving the anomalies are similar to those for the non-upwelling related LSE discussed in the previous paragraph. The combined nTA and S+Fw anomalies (-260 μatm on 15 June and -108 μatm on 5 September) are partially compensated by nDIC contribution (171 μatm and 22 μatm respectively). Unlike for the previous events, we do see a significant temperature effect for the upwelling-related LSE: temperature-generated anomalies are positive (45 μatm on 15 June and 53 μatm on 5 September) and support nDIC contribution.

When following Turi et al. (2014) (Fig. 6e), all LSE, with the exception of the 5 September LSE, are characterized by strong negative solubility-generated anomalies (-163 μatm on 15 March, -78 μatm on 6 May and -55 μatm on 15 June) partially compensated by positive aeration-generated anomalies (65 μatm , 97 μatm and 8 μatm respectively). The odd one out which take place on 5 September shows positive solubility-generated anomaly (27 μatm) and negative aeration-generated anomaly (-30 μatm). In all the four LSE, biological processes did not have any significant impact on $p\text{CO}_2$ variations (anomalies generated by biological processes are 2 to 3 times lower than those generated by aeration or solubility).

4 Discussion

4.1 Impact of Rhône River inputs on TA variations

Due to its location near the Rhône River mouth, the BoM is particularly affected by freshwater inputs. In 2017, there were four LSE in the BoM. Apart from being low in salinity, the Rhone River water entering the BoM also contains organic matter, nutrients, DIC and alkalinity, with a mean TA of 2885 $\mu\text{mol kg}^{-1}$ (Schneider et al., 2007). This input adds up to the

effect of biological processes. We have seen that TA measurements in the BoM exhibit significant variability throughout the year (Fig. 4a), although no obvious seasonality. By considering autochthonous (i.e., dependant on biological processes only) and allochthonous (i.e., dependant on rivers inputs only) formulations of TA, we were able to isolate the effects of the biology and riverine inputs and quantify their relative importance for the TA variations seen in the BoM.

With the autochthonous formulation, TA remained fairly constant throughout the year, which is similar to the results obtained by Lajaunie-Salla et al. (2021). In contrast, the allochthonous formulation produced a much high variability in TA that was close to in situ observations. Several authors suggested that biological processes could have a large effect on TA dynamics in coastal areas (Krumins et al., 2013; Gustafsson et al., 2014). These findings are not confirmed by our model results where changes in TA due to biology did not exceed 5 $\mu\text{mol kg}^{-1}$ (Fig. 4a), which is insignificant compared to the changes attributed to other drivers, including riverine inputs. This suggests that TA variations in the BoM are mostly driven by allochthonous factors. The importance of allochthonous contributions to TA variations have already been highlighted by several authors at the Mediterranean Sea scale (Copin-Montegut, 1993; Schneider et al., 2007; Hassoun et al., 2015). Other important drivers in the Mediterranean include TA exchanges with the Atlantic Ocean and Black Sea, as well as TA inputs from sediments and rain. For the particular location of our study area, we only considered river contributions. Having neglected other allochthonous drivers seems to be justified by the results which showed a close match to observations and a generally better representation of the other carbonate system variables since DIC, $p\text{CO}_2$ and pH_T are all closely related to TA (Fig. 4 and Table 3). Several studies of TA variations in the Mediterranean Sea have been conducted at the sub-basins scale yielding different TA-S correlation for different study areas (Cossarini et al., 2015; Hassoun et al., 2015). For instance, the correlation proposed for the north-western Mediterranean Sea, suggests that local TA dynamics are mainly controlled by evaporation. We did not include this in our study as the BoM is strongly impacted by the Rhône River. By focussing on a smaller area, we could provide a TA formulation that represents this particular part of the Mediterranean very well.

While our results seem to provide a realistic representation of TA dynamics in the BoM, we could have included other factors such as sediments, which have been shown to be important for TA dynamics, particularly in coastal areas (Brenner et al., 2016; Gustafsson et al., 2014). We plan to add TA supplies by sediments in our future work.

4.2 Impact of hydrodynamic processes on $p\text{CO}_2$ variations

4.2.1 Low salinity events (LSE)

The four LSE observed in 2017 had several common characteristics: a salinity decrease (Fig. 6a) and apparent nTA and nDIC increases (Fig. 6b). Three of the four LSE resulted in a $p\text{CO}_2$ decrease (15 March, 6 May, and 15 June, Fig. 6c). Rhône River intrusion events are often associated with a $p\text{CO}_2$ decrease since the introduced nutrients stimulate phytoplanktonic growth (Frayse et al., 2014; Lajaunie-Salla et al., 2021). However, in our case, the decrease of $p\text{CO}_2$ observed on 15 March, 6 May and 15 June was entirely caused by nTA and solubility effects (Figs. 6d,e). Generally, a TA increase is associated with a $p\text{CO}_2$ decrease that is proportional to the buffering state of the considered water mass (for high TA:DIC ratios,

changes in $p\text{CO}_2$ are lower since the water mass is well buffered; Middelburg et al., 2020), which explains the negative $p\text{CO}_2$ anomalies associated with these three LSE. Solubility depends on both salinity and temperature. Depending on the size and the duration of the Rhône River intrusion, salinity effect to solubility can vary. When salinity is decreasing, the solubility of CO_2 in seawater also decreases, which results in a decrease in $p\text{CO}_2$ (Middelburg, 2019). The effects of temperature to solubility vary throughout the year. For instance, during the 15 March and 6 May LSE, temperatures were low and fairly constant (Fig. 6a) and therefore only contributed a small amount to the negative anomaly (Fig. 6d). In contrast, the 15 June, temperature cause a positive $p\text{CO}_2$ anomaly (Fig. 6d). This difference can be explained by the fact that the 15 June LSE took place right after an upwelling event, probably facilitated by the Marseille eddy presence near the BoM, which tend to be observed just after Mistral events (Frayssé et al., 2014). While the temperature dropped as a result of the upwelling, once the event was over the temperature increased again which caused the observed positive $p\text{CO}_2$ anomaly. Despite this positive temperature-related anomaly, the overall anomaly remained negative due to the strong effects of salinity and nTA during the LSE (Fig. 6c).

The 5 September LSE was associated with a $p\text{CO}_2$ increase (Fig. 6c), caused by nDIC and solubility effects (Figs. 6d,e): as salinity and nTA contributions remain weak, they are completely counterbalanced by nDIC and temperature contribution, resulting in an increase of $p\text{CO}_2$. During September 5th LSE, observed salinity and temperature showed opposite patterns: the decrease of salinity is associated to an increase of temperature, and the increase of salinity after the peak of the LSE, is associated to a temperature decrease (Fig. 6a). Unlike for the 15 June LSE, the temperature increase seen during the 5 September event was not caused by the end of the upwelling event preceding as the temperature was decreasing right after the LSE peak (Fig. 6a). We assume that this temperature increase was instead caused by the intruding Rhône River water, which brought about the observed $p\text{CO}_2$ increase ($p\text{CO}_2$ increases exponentially with temperature; Middelburg, 2019).

In all four LSE, biological processes did not have any significant impact on $p\text{CO}_2$ variations (Fig. 6e). To interpret this result, it is important to consider the assumptions used by Eco3M_MIX-CarbOx (section 2.2). Rhône River intrusion can significantly modify the biogeochemistry of the bay as they are typically associated with temperature and salinity changes and TA, DIC and nutrients inputs (Gatti et al., 2006; Frayssé et al., 2014; Lajaunie-Salla et al., 2021). Due to its 0D configuration, Eco3M_MIX-CarbOx only represents temperature and salinity changes and TA inputs (only if the allochthonous formulation is used for the latter, Fig. 2). Lajaunie-Salla et al. (2021) showed that these nutrient inputs led to an increase in chlorophyll concentration. This phytoplankton growth leads to further decrease in $p\text{CO}_2$, which means that by neglecting nutrient inputs we possibly underestimated the importance of biological processes, and especially of autotrophic processes during Rhône River intrusions.

Moreover, the high DIC concentrations observed in Rhône River waters ($2995 \pm 575 \mu\text{M}$ on average, Sempere et al., 2000) could also affect $p\text{CO}_2$ variations by increasing the nDIC contribution during intrusion events which counteract the overall decrease of $p\text{CO}_2$ that is typically observed during these events.

4.2.2 Summer upwelling period (SUP)

During the SUP, regardless of whether there is an LSE, $p\text{CO}_2$ variations mostly depend on temperature and nDIC which tend to produce anomalies of opposite signs (Fig. 6d). Temperature was highly variable during the SUP due to the succession of upwelling events which explains its significant contribution to $p\text{CO}_2$ variations. nDIC contribution can be defined as the sum of aeration and biological processes contributions. During the SUP, biological processes represent 29 % of DIC variations (with 14 % attributed to primary production and 15 % to respiration; results not shown). The remaining 71 % are contributions by aeration. While the contribution of aeration decreased during summer, this decrease was compensated by a 9 % increase in the contribution by biological processes (Fig. 6e). The maximum negative anomaly generated by biological processes occurred at the beginning of the SUP, on 31 May (Fig. 6e), evidence that biological processes and more precisely autotrophic processes are enhanced during late spring. This feature is explained by the change in organisms' limitations. At the end of spring, organisms are less limited by temperature and light. Nevertheless, the overall contribution of biological processes was low compared to aeration and temperature ones. This agrees with observations by Wimart-Rousseau et al. (2020) and Lajaunie-Salla et al. (2021) who showed that, $p\text{CO}_2$ variations and associated CO_2 fluxes are mostly driven by temperature in the BoM.

We showed that upwelling events were associated with strong decreases in $p\text{CO}_2$ (Fig. 6c) mostly as a result of temperature changes. The associated decrease in temperature further decreased $p\text{CO}_2$. This feature is only observed during upwelling events in summer when both temperatures and $p\text{CO}_2$ are high (Figs. 6a,c), stressing the importance of upwelling events for these variables. During upwelling events, aeration-generated anomalies change sign and become positive (Fig. 6e). The observed decrease in temperature resulted in a decrease in seawater $p\text{CO}_2$ to below atmospheric levels, thereby facilitating the absorption of atmospheric CO_2 which caused the reversal sign of aeration-generated anomaly. During upwelling events, the contribution by biological processes is low compared to temperature and aeration which both varied significantly (Fig. 6e). While upwelling events only occur at very specific locations (Côte Bleue and Calanques de Marseille) in our study area, they impact the temperature of the entire BoM (Pairaud et al., 2011). Although upwelling events also bring nutrients and DIC to the surface, these effects are not represented in the Eco3M_MIX-CarbOx model. We can therefore only assume that the nutrient inputs by promoting primary production (Frayssé et al., 2013), would increase the contribution of biological processes (especially of autotrophic processes) resulting in a stronger decrease in $p\text{CO}_2$. However, while DIC inputs would increase the importance of nDIC thereby reducing the decrease of $p\text{CO}_2$ associated with these events.

4.3 Air-sea CO_2 fluxes

We have shown that air-sea CO_2 fluxes oscillated between -13 and 15 mmol m^{-2} per day (Fig. 5d) which is a range similar to the one obtained by Wimart-Rousseau et al. (2020) (-15 and 10 mmol m^{-2} per day) suggesting that our model correctly represents the range of variations of air-sea CO_2 daily fluxes values during the year. CO_2 sinks associated to upwelling events (Lajaunie-Salla et al., 2021) are reproduced by our model. By calculating the daily mean value of air-sea CO_2 fluxes

during the SUP, we obtained a positive value of 0.15 mmol m⁻² per day (or 24.2 mmol m⁻² for the entire SUP). To examine this result in more detail, we performed a sensitivity analysis of our air-sea CO₂ flux calculation (see Appendix E for details) which allowed us to identify the contributions of all relevant parameters (Table 5).

Table 5. Results of the sensitivity analysis showing the effect of varying the relevant parameters by 10%.

	Temperature		Salinity		Wind speed		<i>p</i> CO ₂ difference	
	+10 %	-10 %	+10 %	-10 %	+10 %	-10 %	+10 %	-10 %
Air-sea CO₂ flux difference (mmol m⁻² d⁻¹)	0.016	-0.017	0.044	-0.045	-0.440	0.398	-0.210	0.210

On average, air-sea CO₂ fluxes values during the SUP were mostly driven by wind speed term followed by sea-air *p*CO₂ difference, salinity and finally temperature. According to Eq. (5), wind speed, salinity, and temperature only affect the magnitude of air-sea CO₂ fluxes while their sign is determined by the sea-air *p*CO₂ difference which also impacts their magnitude significantly (Table 5). We have shown that, during the SUP, this difference is mostly driven by temperature since seawater *p*CO₂ variations are controlled by temperature at this time (Figs. 6d,e). A realistic representation of seawater *p*CO₂ is crucial to calculate air-sea CO₂ fluxes. Since seawater *p*CO₂ variations were correctly represented by the model during the SUP (Fig. 4c), the modelled air-sea CO₂ fluxes during the SUP should be reliable.

Over the entire year, air-sea CO₂ fluxes in the BoM essentially evened out yielding only a slightly negative balance of -0.21 mmol m⁻² per year. This is much lower than the -803 mmol m⁻² per year suggested by Wimart-Rousseau et al. (2020). The reason for this discrepancy may be related to the fact that our model overestimates seawater *p*CO₂ during winter, resulting in a sea-air difference close to zero (Fig. 5d). As a result, despite strong winds and low temperatures which would favour CO₂ absorption (Middelburg, 2019), the winter CO₂ sink is not well represented.

Seawater *p*CO₂, air-sea CO₂ fluxes and DIC are closely connected (Appendix B, Fig. 3). In Eco3M_MIX-CarbOx, aeration is simulated by applying Eq. (5) to 1 m³ of surface water at SOLEMIO station which tends to overestimate the impact of aeration process on DIC and, due to the close link between DIC and *p*CO₂, also on *p*CO₂. A simple solution to overcome this problem would be to increase the volume in which aeration process is simulated. However, to be consistent with the representation of other fluxes and the dimensionless concept, increasing the volume would require switching from a 0D to a 1D model minimum, which is planned for our future work.

Most studies that investigated air-sea CO₂ fluxes and other carbonate system variables in various Mediterranean locations at different locations (Ligurian Sea, North Adriatic Sea, BoM) were based on measurements only and concluded that their study areas acted as CO₂ sinks during their study periods (e.g., Begovic, 2003; De Carlo et al., 2013; Ingrosso et al., 2016; Urbini et al., 2020; Wimart-Rousseau et al., 2020). To the best of our knowledge, the only other study examining air-sea CO₂ fluxes in the BoM using a modelling approach was conducted by Lajaunie-Salla et al. (2021) using Eco3m-CarbOx model, which is also dimensionless and based on a 1 m³ volume like Eco3M_MIX-CarbOx and therefore also tend to underestimate the yearly fluxes. Most modelling studies have focussed on larger scales and employed at least 1D models. For instance,

D'Ortenzio et al. (2008), used a coupled 1D model, and found that the Mediterranean Sea, as a whole, was nearly balanced as the western and eastern basins act as CO₂ sink and a source, respectively, and therefore cancel each other out. Using a 3D coupled model and looking at even larger scales, Bourgeois et al. (2016) provided a complete analysis of the air-sea CO₂ fluxes in various coastal environments and have shown that they represent 4.5 % of the anthropogenic CO₂ uptake of the global ocean. 3D models typically allow more realistic representations of the water column, they would allow us to (i) consider a more realistic water volume to perform our air-sea CO₂ fluxes calculation, (ii) consider autochthonous and allochthonous contributions to TA variations, (iii) consider the effects of nutrients and DIC inputs from the Rhône River intrusions and local upwellings. Nevertheless, dimensionless model also offers some advantages such as short simulation time, easy adaptability to as only the forcings need to be modified.

5 Conclusion

Using the concept of the dimensionless Eco3M-CarbOx biogeochemical model as a starting point, we developed a new planktonic ecosystem model which contains, in addition to mixotroph organisms, a modified version of the carbonate module described by Lajaunie-Salla et al. (2021), to represent the carbonate system variables more realistically. First, we improved the parametrisation of TA by developing two different formulations: (i) an autochthonous formulation that only considers biological contributions to TA variations and (ii) an allochthonous formulation that only depends on salinity, thus considers riverine contributions to TA variations. A comparison of both TA formulations showed that TA variations in the BoM were mostly due to allochthonous contributions. Then, we adapted the allochthonous formulation for modelling TA variations in the BoM which, yielded a helpful tool to complement the low frequency in situ measurements. We use this new formulation to study air-sea CO₂ fluxes and seawater *p*CO₂ variations at SOLEMIO station in 2017, focussing on two hydrodynamic processes that are typical for the BoM: (i) Rhône River intrusions and (ii) summer upwelling events.

During the SUP, our model represented the CO₂ sinks generated by summer upwelling events which are suggested by Lajaunie-Salla et al., (2021), and identified the underlying drivers of CO₂ variability. Furthermore, our model was able to simulate the expected decrease in *p*CO₂ associated with summer upwelling events (Lajaunie-Salla et al., 2021). This decrease was mainly generated by temperature effects on *p*CO₂. LSE were also represented by the model. They often generated a decrease in *p*CO₂ as a result of the decreasing salinity and increasing TA, especially when those two contributions were not counterbalanced by temperature effects. However, in winter, the model was unable to reproduce the undersaturation seen in seawater *p*CO₂ measurements at SOLEMIO station and rather overestimate it. As a result, the commonly observed seasonality of air-sea CO₂ fluxes in the north-western Mediterranean was not reproduced by our model which directly impacted our estimates of the overall yearly air-sea CO₂ flux. While correctly identifying the BoM as an overall sink of CO₂, our model significantly underestimated the magnitude (our model : -0.21 mmol m⁻² per year, Wimart-Rousseau et al., (2020): -803 mmol m⁻² per year).

The present work clearly highlighted the limitations of dimensionless models. Although this type of model possesses some advantages that facilitate an improved understanding of complex coastal systems, it has clear limitations when it comes to the representation of specific processes or variables with obvious impacts on the results. The accuracy could be improved by employing a 3D coupled model which would allow us to (i) improve our representation of air-sea CO₂ fluxes by applying them to the whole water column, (ii) improve our representation of TA by considering autochthonous and other allochthonous sources and (iii) improve our representation of LSE and upwelling events by allowing us to consider the inputs of nutrients and DIC.

Appendix A: State equations processes description

Table A1. Description of state equation processes.

Notation	Process
Copepods	
$Excr_{NutX}^{COPX}$ $NutX \in [NH_4^+, PO_4^{3-}]$ $X \in [N, P]$	Excretion of nutrient X by copepods
$Excr_{DOC}^{COPc}$	DOC excretion by copepods
$Resp_{DIC}^{COPc}$	Copepods respiration
E_{POX}^{COPX} $X \in [C, N, P]$	Copepods egestion
$Predation_{POX}^{COPX}$ $X \in [C, N, P]$	Predation by higher trophic levels on copepods
Mixotrophs (Mix \in [NCM, CM])	
$Exu_{DOX}^{MixX_i}$ $X \in [C, N, P]$	DOX exudation by mixotrophs
$Resp_{DIC}^{Mixc}$	Mixotrophs respiration
$Photo_{DIC}^{Mixc}$	Mixotrophs photosynthesis
$Excr_{NutX}^{NCMX}$ $NutX \in [NH_4^+, PO_4^{3-}]$ $X \in [N, P]$	Excretion of nutrient X by NCM
Upt_{NutX}^{CMX} $X \in [N, P]$ $NutX \in [NO_3^-, NH_4^+, PO_4^{3-}]$	Uptake of nutrient X by constitutive mixotrophs
Upt_{DOX}^{CMX} $X \in [N, P]$	Uptake of DOX by constitutive mixotrophs
Phytoplankton (Phy \in [NMPHYTO, PICO])	
$Resp_{DIC}^{Phyc}$	Phytoplankton respiration
$Photo_{DIC}^{Phyc}$	Phytoplankton photosynthesis
Upt_{NutX}^{PhyX} $NutX \in [NO_3^-, NH_4^+, PO_4^{3-}]$	Uptake of nutrient X by phytoplankton
Exu_{DOX}^{PhyX} $X \in [C, N, P]$	DOX exudation by phytoplankton
Upt_{DOX}^{PICOX} $X \in [N, P]$	Uptake of DOX by picophytoplankton
Heterotrophic bacteria	
BP_X^{BACc}	Bacterial production

$X \in [\text{DOC}, \text{POC}]$	
$\text{BR}_{\text{DIC}}^{\text{BACc}}$	Bacterial respiration
$\text{Upt}_{\text{POX}}^{\text{BACX}}$	POX uptake by heterotrophic bacteria
$X \in [\text{N}, \text{P}]$	
$\text{Exu}_{\text{DOX}}^{\text{PhyX}_i}$	DOX exudation by phytoplankton
$X \in [\text{C}, \text{N}, \text{P}]$	
$\text{Remin}_{\text{BACX}}^{\text{NutX}}$	Remineralisation of nutrient X by heterotrophic bacteria
$\text{NutX} \in [\text{NH}_4^+, \text{PO}_4^{3-}]$	
$X \in [\text{N}, \text{P}]$	
$\text{Mort}_{\text{DOX}}^{\text{BACX}}$	Heterotrophic bacteria natural mortality
Dissolved inorganic matter (DIM)	
$\text{Diss}_{\text{DIC}}^{\text{CaCO}_3}$	CaCO_3 dissolution
$\text{Prec}_{\text{DIC}}^{\text{CaCO}_3}$	CaCO_3 precipitation
Nitrif	Nitrification
Aera _{DIC}	Air-sea CO_2 gas exchanges (aeration)

670 **Appendix B: pH_T and pCO₂ calculation**

The calculation method performed in the Eco3M_MIX-CarbOx model to obtain pH_T and pCO₂ is detailed below. As specified in Sect. 2, we used the method introduced by Lajaunie-Salla et al. (2021), which is based on CO2SYSv3 (Sharp et al., 2020), a software originally developed by Lewis and Wallas (1998) to perform the resolution of carbonate system, to perform this calculation. This appendix aims to complete Appendix A from Lajaunie-Salla et al. (2021) by providing some
675 corrections.

B.1 Equilibrium constants and conservative elements concentrations calculation

In the following formulations, S represents the practical salinity.

B.1.1 Conservative elements concentrations and ionic strength

Table B1. Formulations of conservative elements concentrations and ionic strength.

Description	Formulation	Units
Concentration in total fluoride (Riley, 1965)	$TF = \frac{0.000067}{18.998} * \frac{S}{1.80655}$	mol kg ⁻¹
Concentration in total sulfate (Morris & Riley, 1966)	$TS = \frac{0.14}{96.062} * \frac{S}{1.80655}$	mol kg ⁻¹
Concentration in total Boron (Uppström, 1974)	$TB = \frac{0.000416 * S}{35}$	mol kg ⁻¹
Concentration in calcium ion (Riley & Tongudai, 1967)	$Ca^{2+} = \frac{0.02128}{40.087} * \frac{S}{1.80655}$	mol kg ⁻¹
Ionic strength (DOE, 1994)	$IonS = \frac{19.924 * S}{1000 - 1.005 * S}$	∅

680 **B.1.2 Equilibrium constants**

In the following formulations, T represents temperature value converted in Kelvin (i.e., T(°C) + 273.15).

K_F (mol kg⁻¹): HF dissociation constant (Dickson & Riley, 1979)

$$\ln(K_F) = \frac{1590.2}{T} - 12.641 + 1.525 * IonS^{0.5}$$

$$K_F = \exp(\ln(K_F) * (1 - 0.001005 * S))$$

(B1)

685 K_F is expressed on free pH scale.

K_S (mol kg⁻¹): HSO₄⁻ dissociation constant (Dickson, 1990a)

$$\ln(K_S)_{temp} = -\frac{4276.1}{T} + 141.328 - 23.093 * \ln(T) + \left(-\frac{13856}{T} + 324.57 - 47.986 * \ln(T)\right) * IonS^{0.5}$$

$$\ln(K_S) = \ln(K_S)_{temp} + \left(\frac{35474}{T} - 771.54 + 114,723 * \ln(T)\right) * IonS - \frac{2698}{T} * IonS^{1.5} + \frac{1776}{T} * IonS^2$$

$$K_S = \exp(\ln(K_S) * (1 - 0.001005 * S)) \quad (B2)$$

690 K_S is expressed on free pH scale.

K_B (mol kg⁻¹): B(OH)₃ dissociation constant (Dickson, 1990b)

$$\ln(K_B)_{temp} = \frac{-8996.9 - 2890.53 * S^{0.5} - 77.942 * S + 1.728 * S^{1.5} - 0.0996 * S^2}{T} + 148.0248 + 137.1942 * S^{0.5}$$

$$\ln(K_B) = \ln(K_B)_{temp} + 1.62142 * S + (-24.4344 - 25.085 * S^{0.5} - 0.2474 * S) * \ln(T) + 0.053105 * S^{0.5} * T$$

$$K_B = \exp(\ln(K_B)) \quad (B3)$$

695 K_B is expressed on total pH scale.

K_{ca} (mol kg⁻¹)²: Calcite formation constant (Mucci, 1983)

$$\log(K_{ca})_{temp} = -171.9065 - 0.077993 * T + \frac{2839.319}{T} + 71.595 * \log(T)$$

$$\log(K_{ca}) = \log(K_{ca})_{temp} + \left(-0.77712 + 0.0028426 * T + \frac{178.34}{T}\right) * S^{0.5} - 0.07711 * S + 0.0041249 * S^{1.5}$$

$$K_{ca} = 10^{(\log(K_{ca}))} \quad (B4)$$

700 K_e (mol kg⁻¹): H₂O dissociation constant (Millero, 1995)

$$\ln(K_e) = -\frac{13847.26}{T} + 148.9802 - 23.6521 * \ln(T) + \left(-5.977 + \frac{118.67}{T} + 1.0495 * \ln(T)\right) * S^{0.5} - 0.01615 * S$$

$$K_e = \exp(\ln(K_e)) \quad (B5)$$

K_e is expressed on SWS pH scale.

K_0 (mol kg⁻¹ atm⁻¹): CO₂ solubility (Weiss, 1974)

$$705 \ln(K_0)_{temp} = -60.2409 + 93.4517 * \frac{100}{T} + 23.3585 * \ln\left(\frac{T}{100}\right)$$

$$\ln(K_0) = \ln(K_0)_{temp} + S * \left(0.023517 - 0.023656 * \frac{T}{100} + 0.0047036 * \left(\frac{T}{100}\right)^2\right)$$

$$K_0 = \exp(\ln(K_0)) \quad (B6)$$

K_1 (mol kg⁻¹): H₂CO₃ dissociation (Lueker et al., 2000)

$$pK_1 = \frac{3633.86}{T} - 61.2172 + 9.6777 * \ln(T) - 0.011555 * S + 0.0001152 * S^2$$

$$710 K_1 = 10^{(-pK_1)} \quad (B7)$$

K_1 is expressed on total pH scale.

K_2 (mol kg⁻¹): HCO₃⁻ dissociation (Lueker et al., 2000)

$$pK_2 = \frac{471.78}{T} + 25.929 - 3.16967 * \ln(T) - 0.01781 * S + 0.0001122 * S^2$$

$$K_2 = 10^{(-pK_2)}$$

(B8)

715 K_2 is expressed on total pH scale.

B.1.3 pH scale conversion

pH calculation is performed on total scale. Accordingly, the previous constants are converted if necessary (i.e., expressed on total pH scale) using the following conversion factors. Except K_S and K_F which must be expressed on free pH scale, the other equilibrium constants must be converted to total pH scale.

720 **Table B2. Formulation of pH scale conversion factors.**

Description	Conversion factor
From SWS pH scale to total pH scale	$\frac{1 + \frac{T_S}{K_S}}{1 + \frac{T_S}{K_S} + \frac{T_F}{K_F}}$
From free pH scale to total pH scale	$1 + \frac{T_S}{K_S}$

B.1.4 Pressure correction

All the constants are corrected by the effect of hydrostatic pressure using the following formulations (Millero, 1995). We define T_K and T_C which represents respectively the temperature in Kelvin and in Celsius degree. R represents the gas constant in ml bar⁻¹ K⁻¹ mol⁻¹ ($R = 83.1451$ ml bar⁻¹ K⁻¹ mol⁻¹) and P the pressure in bar.

725 Corrected K_F (mol kg⁻¹):

$$K_F CorrFac = \frac{(9.78 + 0.009 * T_C + 0.0009429 * T_C^2 + 0.5 * (\frac{-3.91 + 0.054 * T_C}{1000}) * P) * P}{R * T_K}$$

$$K_F = K_F * \exp(K_F CorrFac)$$

(B9)

Corrected K_S (mol kg⁻¹):

$$K_S CorrFac = \frac{(18.03 - 0.0466 * T_C - 0.000316 * T_C^2 + 0.5 * (\frac{-4.53 + 0.09 * T_C}{1000}) * P) * P}{R * T_K}$$

730 $K_S = K_S * \exp(K_S CorrFac)$

(B10)

Corrected K_B (mol kg⁻¹):

$$K_B \text{CorrFac} = \frac{(29.48 - 0.1622 * T_C + 0.002608 * T_C^2 + 0.5 * (\frac{-2.84}{1000}) * P) * P}{R * T_K}$$

$$K_B = K_B * \exp(K_B \text{CorrFac})$$

(B11)

Corrected K_{ca} (mol kg⁻¹):

$$735 \quad K_{ca} \text{CorrFac} = \frac{(48.76 - 0.5304 * T_C + 0.5 * (\frac{-11.76 + 0.3692 * T_C}{1000}) * P) * P}{R * T_K}$$

$$K_{ca} = K_{ca} * \exp(K_{ca} \text{CorrFac})$$

(B12)

Corrected K_e (mol kg⁻¹):

$$K_e \text{CorrFac} = \frac{(20.02 - 0.1119 * T_C + 0.001409 * T_C^2 + 0.5 * (\frac{-5.13 + 0.0794 * T_C}{1000}) * P) * P}{R * T_K}$$

$$K_e \text{CorrFac} = K_e * \exp(K_e \text{CorrFac})$$

(B13)

740 Corrected K_1 (mol kg⁻¹):

$$K_1 \text{CorrFac} = \frac{(25.5 - 0.1271 * T_C + 0.5 * (\frac{-3.08 + 0.0877 * T_C}{1000}) * P) * P}{R * T_K}$$

$$K_1 = K_1 * \exp(K_1 \text{CorrFac})$$

(B14)

Corrected K_2 (mol kg⁻¹):

$$K_2 \text{CorrFac} = \frac{(15.82 + 0.0219 * T_C + 0.5 * (\frac{1.13 + 0.1475 * T_C}{1000}) * P) * P}{R * T_K}$$

745 $K_2 = K_2 * \exp(K_2 \text{CorrFac})$

(B15)

B.1.5 Fugacity factor

To perform the calculation of the fugacity factor (FugFac), we supposed that the pressure value is close or equal to an atmosphere (Weiss, 1974).

T represents the temperature in Kelvin. We define P_{atm} , as the atmospheric pressure in bar: $P_{atm} = 1.01325$ bar.

$$750 \quad \ln(\text{FugFac}) = \frac{((-1636.75 + 12.0408 * T - 0.0327957 * T^2 + 3.16528 * 0.00001 * T^3) + 2 * (57.7 - 0.118 * T)) * P_{atm}}{R * T}$$

$$\text{FugFac} = \exp(\ln(\text{FugFac}))$$

(B16)

B.2 pH_T and pCO₂ calculation

B.2.1 pH_T calculation

755 As specified in Sect. 2, we obtain the new pH_T value using the buffering value (B). B is defined as the pH variation induced by an addition of acid or base to a considered solution (Van Slycke, 1922). In seawater, the expression of buffering value is based on TA (Middelburg, 2019), the pH_T variation is then, calculated as follows:

$$B = \frac{\partial TA}{\partial pH_T} \Leftrightarrow \Delta pH_T = \frac{\partial TA}{\sum_{i=1}^n B_i}, \quad (\text{B17})$$

where i represents a chemical species contributing to TA.

760 Accordingly, we calculate the pH_T difference between two model time steps (ΔpH_T) using an iterative method. We set the pH_T initial value to 8.0. We chose this value by considering the Mediterranean and Rhône River pH_T which are respectively close and equal to 8.0. Finally, considering that the measurements precision is rather close to 0.0004 (Clayton & Byrne, 1993), we set the tolerance threshold to 0.0001. pH_T calculation is detailed below:

```
! pH initial value = 8.0
! pHTol = Tolerance threshold --> 0.0001
! deltaph = pH difference between two model iterations
! pH is calculated on total scale

if (nbIter < 1) pH = 8.0

pHTol = 0.0001
deltaph = pHTol + 1

do while (abs(deltaph) > pHTol)
  H = 10^(-pH)
  Denom = H^2 + K1 * H + K1 * K2
  CAlk = DIC * K1 * ((H + 2 * K2)/Denom) !Carbonate Alkalinity
  BAlk = (TB * KB)/(KB + H) ! Borate Alkalinity
  OH = Ke/H
  FreeToTot = 1 + (TS/KS)
  HFree = H/FreeToTot
  HSO4 = TS/(1+(KS/HFree))
  HF = TF/(1+(KF/H))
  Residual = TA - CAlk - BAlk - OH + HFree + HSO4 + HF
  Slope = DIC * H * K1 * (H^2 + K1 * K2 + 4 * H * K2)
  Slope = Slope/(Denom^2) + OH + H + (BAlk * H)/(KB + H)
  Slope = log(10) * Slope
  deltaph = Residual/Slope

  do while (abs(deltaph) > 1)
    deltaph = deltaph/2
  enddo

  pH = pH + deltaph
enddo
```

765 **Figure B1: pH_T calculation**

B.2.2 $p\text{CO}_2$ and carbonate system species concentrations

$p\text{CO}_2$ is deducted using DIC, pH (via H^+ concentration) and equilibrium constants. We also calculate the concentrations of CO_2 , HCO_3^- , CO_3^{2-} and CaCO_3 saturation (Ω).

Table B3. Formulation of $p\text{CO}_2$ and carbon system species concentrations.

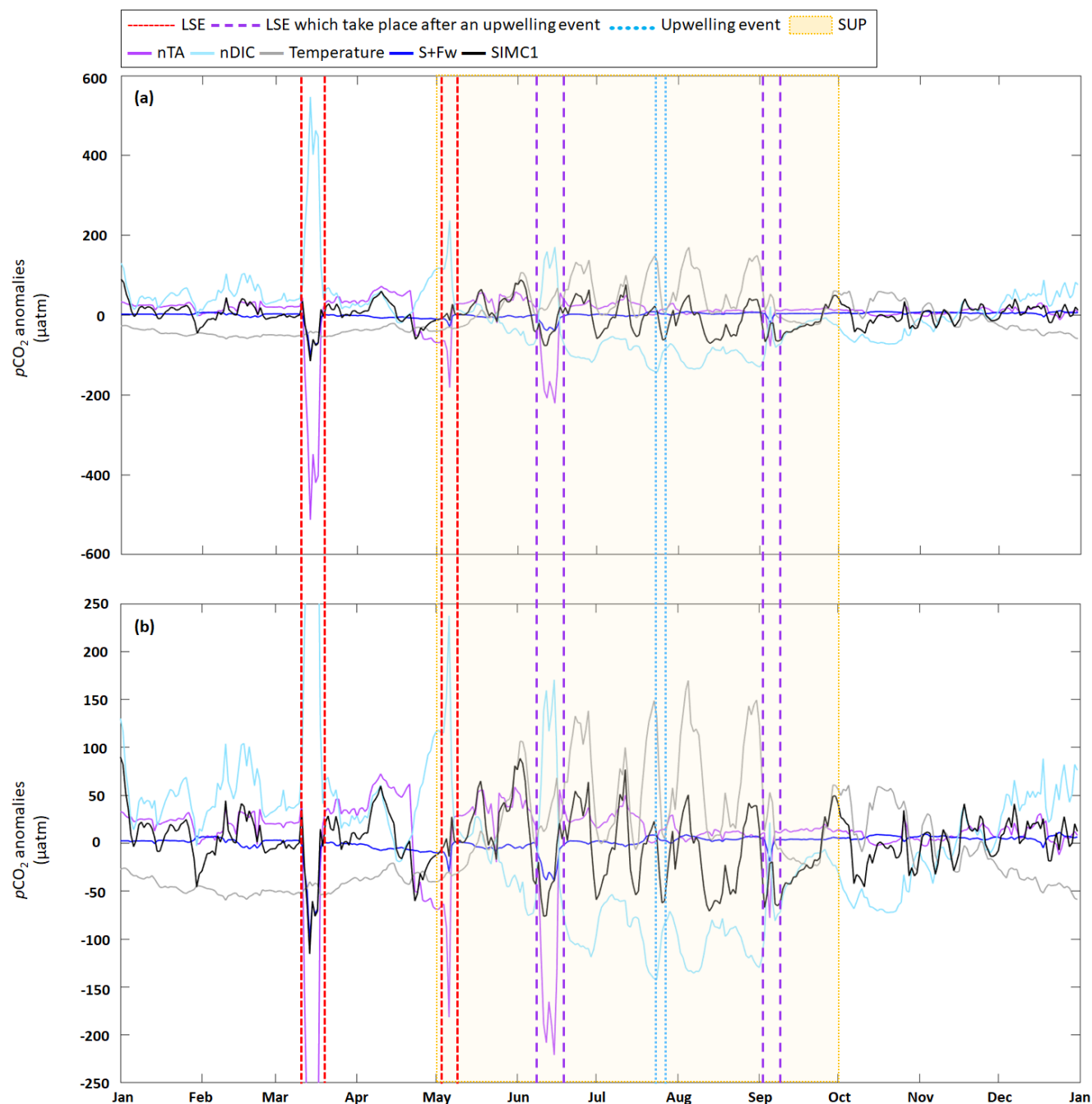
Description	Formulation	Units
$p\text{CO}_2$	$p\text{CO}_2 = \frac{\text{DIC} * [\text{H}^+]^2}{[\text{H}^+]^2 + K_1 * [\text{H}^+] + K_1 * K_2} * \frac{10^6}{K_0 * \text{FugFac}}$	μatm
CO_2 concentration	$[\text{CO}_2^*] = \frac{(\text{DIC} * 10^6)}{\left(1 + \frac{K_1}{[\text{H}^+]} + \frac{(K_1 * K_2)}{[\text{H}^+]^2}\right)}$	$\mu\text{mol kg}^{-1}$
HCO_3^- concentration	$[\text{HCO}_3^-] = \frac{K_1 * [\text{CO}_2^*]}{[\text{H}^+]}$	$\mu\text{mol kg}^{-1}$
CO_3^{2-} concentration	$[\text{CO}_3^{2-}] = \frac{K_2 * [\text{HCO}_3^-]}{[\text{H}^+]}$	$\mu\text{mol kg}^{-1}$
CaCO_3 saturation state	$\Omega = \frac{[\text{Ca}^{2+}] * [\text{CO}_3^{2-}] * 10^{-6}}{K_{ca}}$	\emptyset

Appendix C: Statistic indicators calculation for H⁺ concentration

775 **Table C1:** Comparing the different model results to surface observations at SOLEMIO station for H⁺ concentration. N represents the number of observations. Mean, SD, AE, AAE and RMSD are in the same unit than the considered variable, i.e.: mmol m⁻³ for H⁺ concentrations. % BIAS is without unit.

		[H ⁺]
N	Observations	20
Mean ± SD	Observations	$8.08 \times 10^{-9} \pm 5.52 \times 10^{-10}$
Mean ± SD	SIMC0	$8.89 \times 10^{-9} \pm 2.91 \times 10^{-10}$
	SIMC1	$8.39 \times 10^{-9} \pm 4.06 \times 10^{-10}$
	CarbOx	$8.52 \times 10^{-9} \pm 2.80 \times 10^{-10}$
%BIAS	SIMC0	-5.33
	SIMC1	-3.91
	CarbOx	-5.47
AE	SIMC0	-4.30×10^{-10}
	SIMC1	-3.15×10^{-10}
	CarbOx	-4.42×10^{-10}
AAE	SIMC0	6.45×10^{-10}
	SIMC1	6.05×10^{-10}
	CarbOx	6.36×10^{-10}
RMSD	SIMC0	6.98×10^{-10}
	SIMC1	7.14×10^{-10}
	CarbOx	6.93×10^{-10}

Appendix D: Time series of daily average $p\text{CO}_2$ anomalies generated by DIC, TA, Fw+S and temperature based on the approach described by Lovenduski et al. (2007), for 2017. Enlargement of the panel d, of figure 6.



780

Figure D1. Time series for 2017 of daily average (a) $p\text{CO}_2$ anomalies generated by DIC, TA, Fw+S and temperature based on the approach in Lovenduski et al. (2007) (Note: the dark blue line is sometimes obscured by the black line, especially in March), (b) enlargement of the panel a between -250 and 250 μatm . LSE and an upwelling event have been highlighted. The summer upwelling period (SUP) is indicated by yellow shading.

785 **Appendix E: Sensibility analysis performed on air-sea CO₂ fluxes calculation.**

A sensibility analysis was performed to evaluate the importance of temperature, salinity, wind speed and seawater-atmospheric *p*CO₂ difference terms in the air-sea CO₂ fluxes calculation. Previous terms are one by one increased (decreased) by 10 %. Air-sea CO₂ fluxes are then, post-processed using the Eqs. (8) and (9). Calculation is performed using MATLAB. We present in Table 5 the mean difference between the reference air-sea CO₂ fluxes (i.e., calculated without increasing (decreasing) by 10 % one of the calculation terms) and the air-sea CO₂ fluxes obtained by adding (removing) 10 % to one of the terms of the calculation (Eq. E1).

$$\Delta_{\text{Air-sea CO}_2\text{ Fluxes}} = \frac{1}{N} * \sum_{i=1}^N (\text{abs}(\text{Ref}) - \text{abs}(X_{10\%})), \quad (\text{E1})$$

where $\Delta_{\text{Air-sea CO}_2\text{ Fluxes}}$ is expressed in mmol m⁻² s⁻¹ N is the number of modelled values. X represents temperature, salinity, wind speed or the difference between seawater and atmospheric *p*CO₂

795

Code availability

The current version of Eco3M_MIX-CarbOx is available from the Zenodo website (https://zenodo.org/record/7669658#.Y_dAJ0NKg2w, last access: 23 February 2023) under the Creative Commons Attribution 4.0 international licence. The exact version of the model used to produce the results in this paper is archived on
800 Zenodo (Barré Lucille, Diaz Frédéric, Wagener Thibaut, Van Wambeke France, Mazoyer Camille, Yohia Christophe, & Pinazo Christel. (2022). Eco3M_MIX-CarbOx (v1.0). Zenodo. <https://doi.org/10.5281/zenodo.7669658>), as are input data and scripts to run the model and produce the plots for all the simulation presented in this paper.

Data availability

SOLEMIO time serie data is available on <https://www.seanoe.org>. Temperature data is available on www.t-mednet.org by
805 filling out the request form for station and years pre-selected. Salinity data is available on <https://erddap.osupytheas.fr>. The non-processed atmospheric $p\text{CO}_2$ data can be found on <https://servicedata.atmosud.org/donnees-stations>. Request for processed atmospheric $p\text{CO}_2$ data should be addressed to alexandre.armengaud@airpaca.org and irene.xueref-remy@imbe.fr.

Author contribution

810 LB conceptualized this study, developed the Eco3M_MIX-CarbOx model v1.0, and it, designed the numerical experiments, developed MATLAB software to visualize and process the model results, processed, and analysed the model results, wrote the initial draft. FD provided the initial version of the model code (without carbonate module and with an initial implementation of the mixotroph organisms) and helped to develop the Eco3M_MIX-CarbOx v1.0. TW participated to the conceptualization of this study, participated to the data acquisition of carbonate variables, helped to design the numerical
815 experiments, analysed the model results, reviewed, and edited the initial draft. CM helped in the model development process by giving expertise on the code development to reduce calculation time. CY provided the wind and irradiance data, maintained computing resources. CP acquired the fundings, participated to the conceptualization of this study and supervised it, participated to the model development, designed the numerical experiments, analysed the model results, and reviewed and edited the initial draft.

820 Competing interests

The authors declare that they have no conflict of interest.

Acknowledgements

We thank the National Service d'Observation en MILieu Littoral (SOMLIT) for its permission to use SOLEMIO data. We would like to thank the crew members of the RV Antedon II, operated by the DT-INSU, for making these samplings possible, the team of the SAM platform (Service Atmosphère Mer) of the MIO for help with the field work. We also thank Michel Lafont and Véronique Lagadec of the PACEM (Plateforme Analytique de Chimie des Environnements Marins) platform of the MIO and the SNAPO-CO₂ at LOCEAN, Paris. The SNAPO-CO₂ service at LOCEAN is supported by CNRS-INSU and OSU Ecce-Terra. We acknowledge the TMEDNet team for its permission to use the Planier-Souquet temperature data. We thank the ROMARIN network team for its permission to use the salinity data from Carry buoy. We thank the observatoire de la qualité de l'air en Région Sud Provence-Alpes-Côte d'Azur (ATMOSUD) in particular, Alexandre Armengaud, and the AMC (Aix-Marseille Carbon Pilot Study) project leaders, Irène Xueref-Remy and Dominique Lefèvre for providing the atmospheric CO₂ data at the Cinq Avenue station. We acknowledge the staff of the "Cluster de calcul intensif HPC" platform of the OSU Institut PYTHEAS (Aix-Marseille Université, INSU-CNRS) for providing the computing facilities. We would like to thank Julien Lecubin from the Service Informatique de l'OSU Institut Pytheas for its technical assistance. We thank XpertScientific team for the manuscript correction.

Fundings

This work takes part of the IAMM project (Évaluer l'Impact de la métropole Aix-Marseille sur l'Acidification de la baie de Marseille et les conséquences sur les microorganismes marins, approche par Modélisation) funded by the public establishment of the Ministry of the Environment, l'Agence de l'eau Rhône Méditerranée Corse.

References

- Allen, J. I., Holt, J. T., Blackford, J. and Proctor, R.: Error quantification of a high-resolution coupled hydrodynamicecosystem coastal-ocean model: Part 2. Chlorophyll-a, nutrients and SPM, *Journal of Marine Systems*, 68, 381-404, <https://doi.org/10.1016/j.jmarsys.2007.01.005>, 2007.
- Artioli, Y., Blackford, J. C., Nondal, G., Bellerby, R. J. G., Wakelin, S. L., Holt, J. T., Butenschön, M. and Allen, I. J.: Heterogeneity of impacts of high CO₂ on the North-western European Shelf, *Biogeosciences*, 11, 601-612, <https://doi.org/10.5194/bg-11-601-2014>, 2014.
- Baklouti, M., Faure, V., Pawlowski, L., and Sciandra, A.: Investigation and sensitivity analysis of a mechanistic phytoplankton model implemented in a new modular numerical tool (Eco3M) dedicated to biogeochemical modelling, *Prog. Oceanogr.*, 71, 34–58, <https://doi.org/10.1016/j.pocean.2006.05.003>, 2006a.

- 850 Baklouti, M., Diaz, F., Pinazo, C., Faure, V. and Queguiner, B.: Investigation of mechanistic formulations depicting phytoplankton dynamics for models of marine pelagic ecosystems and description of a new model, *Prog. Oceanogr.*, 71, 1-33, <https://doi.org/doi:10.1016/j.pocean.2006.05.002>, 2006b.
- Barré, L., Diaz, F., Wagener, T., Van Wambeke, F., Mazoyer, C., Yohia, C. and Pinazo, C.: Implementation and assessment of a model including mixotrophs and the carbonate cycle (Eco3M_MIX-CarbOx v1.0) in a highly dynamic Mediterranean coastal environment (Bay of Marseille, France) (Part I): Evolution of ecosystem composition under limited light and nutrient conditions, <https://doi.org/10.5194/gmd-16-6701-2023>, 2023.
- Barrier, N., Petrenko, A. A. and Ourmières, Y.: Strong intrusions of the Northern Mediterranean Current on the eastern Gulf of Lion: insights from in-situ observations and high-resolution numerical modelling, *Ocean Dynamics*, 66, 313–327, <https://doi.org/10.1007/s10236-016-0921-7>, 2016.
- 860 Bates, N. R., Best, M. H. P., Neely, K., Garley, R., Dickson, A. G. and Johnson, R. J.: Detecting anthropogenic carbon dioxide uptake and ocean acidification in the North Atlantic Ocean, *Biogeosciences*, 9, 2500-2522, <https://doi.org/10.5194/bg-9-2509-2012>, 2012.
- Begovic, M.: Contribution à l'étude du système des carbonates en Méditerranée-Distribution et variation spatio-temporelle de la pression partielle de CO₂ dans les eaux superficielles du bassin Liguro-Provençal, Ph.D. Thesis, Université Pierre et Marie Curie - Paris VI, 2001.
- 865 Bourgeois, T., Orr, J. C., Resplandy, L., Terhaar, J., Ethé, C., Gehlen, M. and Bopp, L.: Coastal-ocean uptake of anthropogenic carbon, *Biogeosciences*, 13, 4167-4185, <https://doi.org/10.5194/bg-13-4167-2016>, 2016.
- Brenner, H., Braeckman, U., Le Guitton, M. and Meysman, F. J. R.: The impact of sedimentary alkalinity release on the water column CO₂ system in the North Sea, *Biogeosciences*, 13, 841-863, <https://doi.org/10.5194/bg-13-841-2016>, 2016.
- 870 Carstensen, J., Chierci, M., Gustafsson, B. G. and Gustafsson, E.: Long-term and seasonal trends in estuarine and coastal carbonate systems, *Global Biogeochemical Cycles*, 32, 497–513, <https://doi.org/10.1002/2017gb005781>, 2018.
- Copin-Montegut, C.: Alkalinity and carbon budgets in the Mediterranean Sea, *Global Biogeochemical Cycles*, 7, 915-925, <https://doi.org/10.1029/93GB01826>, 1993.
- Cossarini, G., Lazzari, P. and Solidoro, C.: Spatiotemporal variability of alkalinity in the Mediterranean Sea, *Biogeosciences*, 12, 1645-1658, <https://doi.org/10.5194/bg-12-1647-2015>, 2015.
- 875 Crossland, C. J., Baird, D., Ducrottoy, J.-P. and Lindeboom, H. J.: The coastal zone, a domain of global interactions, *Coastal Fluxes in the Anthropocene*, *Global Change – The IGBP Series*, Springer-Verlag, pp 1-38, 2005.
- De Carlo, E. H., Mousseau, L., Passafiume, O., Drupp, P. S. and Gattuso, J. -P.: Carbonate Chemistry and Air–Sea CO₂ Flux in a NW Mediterranean Bay Over a Four-Year Period: 2007–2011, *Aquatic Geochemistry*, 19, 399-442, <https://doi.org/10.1007/s10498-013-9217-4>, 2013.
- 880 Dickson, A. G.: Standard potential of the reaction: AgCl(s) + 1/2 H₂(g) = Ag(s) + HCl(aq), and the standard acidity constant of the ion HSO₄⁻ in synthetic seawater from 273.15 to 318.15 K, *Journal of Chemical Thermodynamics*, 22, 113-127, 1990a.

- Dickson, A. G.: Thermodynamics of the dissociation of boric acid in synthetic seawater from 273.15 to 318.15 K, *Deep-Sea Research*, 37, 755–766, [https://doi.org/10.1016/0198-0149\(90\)90004-F](https://doi.org/10.1016/0198-0149(90)90004-F), 1990b.
- 885 Dickson, A. G. and Riley, J. P.: The estimation of acid dissociation constants in seawater media from potentiometric titrations with strong base. I. The ionic product of water – KW, *Marine Chemistry*, 7, 89-99, 1979a.
- Dickson, A. G. and Riley, J. P.: The estimation of acid dissociation constants in sea-water media from potentiometric titrations with strong base. II. The dissociation of phosphoric acid, *Marine Chemistry*, 7, 101–109, [https://doi.org/10.1016/0304-4203\(79\)90002-1](https://doi.org/10.1016/0304-4203(79)90002-1), 1979b.
- 890 DOE (U.S. Department of Energy): Handbook of methods for the analysis of the various parameters of the carbon dioxide system in seawater; version 2. A.G. Dickson, and C. Goyet, eds. ORNL/CDIAC-74, 1994.
- Dore, J. E., Lukas, R., Sadler, D. W., Church, M. J. and Karl, D. M.: Physical and biogeochemical modulation of ocean acidification in the central North Pacific, *Proceedings of the National Academy of Sciences*, 106, 12235-12240, <https://doi.org/10.1073/pnas.0906044106>, 2009.
- 895 D’Ortenzio, F., Antoine, D. and Marullo, S.: Satellite-driven modeling of the upper ocean mixed layer and air–sea CO₂ flux in the Mediterranean Sea, *Deep Sea Research*, 55 (4), 405-434, <https://doi.org/10.1016/j.dsr.2007.12.008>, 2008.
- Feely, R. A., Doney, S. C. and Cooley, S. R.: Ocean Acidification: Present conditions and future changes in a high-CO₂ world, *Oceanography*, 22(4), 36-47, 2009.
- Frayse, M., Pinazo, C., Faure, V. M., Fuchs, R., Lazzari, P., Raimbault, P. and Peyraud, I.: Development of a 3D Coupled
 900 Physical-Biogeochemical Model for the Marseille Coastal Area (NW Mediterranean Sea): What Complexity Is Required in the Coastal Zone? *PLoS ONE*, 8(12): e80012, <https://doi.org/10.1371/journal.pone.0080012>, 2013.
- Frayse, M., Pairaud, I., Ross, O. N., Faure, V. M. and Pinazo, C.: Intrusion of Rhone River diluted water into the Bay of Marseille: Generation processes and impacts on ecosystem functioning, *Journal of Geophysical Research: Oceans*, 119, <https://doi.org/10.1002/2014JC010022>, 2014.
- 905 Friedlingstein, P., Jones, M. W., O’Sullivan, M., Andrew, R. M., Bakker, D. C. E., Hauck, J., Le Quéré, C., Peters, G. P., Peters, W., Pongratz, J., Sitch, S., Canadell, J. G., Ciais, P., Jackson, R. B., Alin, S. R., Anthoni, P., Bates, N. R., Becker, M., Bellouin, N., Bopp, L., Chau, T. T. T., Chevallier, F., Chini, L. P., Cronin, M., Currie, K. I., Decharme, B., Djeutchouang, L. M., Dou, X., Evans, W., Feely, R. A., Feng, L., Gasser, T., Gilfillan, D., Gkritzalis, T., Grassi, G., Gregor, L., Gruber, N., Gurses, O., Harris, I., Houghton, R. A., Hurtt, G. C., Iida, Y., Ilyina, T., Luijkx, I. T., Jain, A., Jones, S. D.,
 910 Kato, E., Kennedy, D., Klein Goldewijk, K., Knauer, J., Korsbakken, J. I., Körtzinger, A., Landschützer, P., Lauvset, S. K., Lefèvre, N., Lienert, S., Liu, J., Marland, G., McGuire, P. C., Melton, J. R., Munro, D. R., Nabel, J. E. M. S., Nakaoka, S.-I., Niwa, Y., Ono, T., Pierrot, D., Poulter, B., Rehder, G., Resplandy, L., Robertson, E., Rödenbeck, C., Rosan, T. M., Schwinger, J., Schwingshackl, C., Séférian, R., Sutton, A. J., Sweeney, C., Tanhua, T., Tans, P. P., Tian, H., Tilbrook, B., Tubiello, F., van der Werf, G. R., Vuichard, N., Wada, C., Wanninkhof, R., Watson, A. J., Willis, D., Wiltshire, A. J., Yuan,
 915 W., Yue, C., Yue, X., Zaehle, S. and Zeng, J.: Global Carbon Budget 2021, *Earth System Science Data*, 14, 1917-2005, <https://doi.org/10.5194/essd-14-1917-2022>, 2022.

- Gatti, J., Petrenko, A., Devenon, J. -L., Leredde, Y. and Ulses, C.: The Rhone River dilution zone present in the northeastern shelf of the Gulf of Lion in December 2003, *Continental Shelf Research*, 26, 1794-1815, <https://doi.org/10.1016/j.csr.2006.05.012>, 2006.
- 920 Gattuso, J. -P., Frankignoulle, M. and Wollast, R.: Carbon and carbonate metabolism in coastal aquatic ecosystems, *Annual Review of Ecology, Evolution, and Systematics*, 29, 405–34, <https://doi.org/10.1146/annurev.ecolsys.29.1.405>, 1998.
- Gonzales-Dávila, M., Santana-Casiano, J. M., Rueda, M. J. and Llinás, O.: The water column distribution of carbonate system variables at the ESTOC site from 1995 to 2004, *Biogeosciences*, 7, 3067-3081, <https://doi.org/10.5194/bg-7-3067-2010>, 2010.
- 925 Guerzoni, S., Molinaroli, E. and Chester, R.: Saharan dust inputs to the western Mediterranean Sea: depositional patterns, geochemistry and sedimentological implications, *Deep Sea Research Part II: Topical Studies in Oceanography*, 44(3-4), 631-654, [https://doi.org/10.1016/S0967-0645\(96\)00096-3](https://doi.org/10.1016/S0967-0645(96)00096-3), 1997.
- Gustafsson, E., Wällstedt, T., Humborg, C., Mörtz, C. -M. and Gustafsson, B. G.: External total alkalinity loads versus internal generation: The influence of nonriverine alkalinity sources in the Baltic Sea, *Global Biogeochemical Cycles*, 28, 1358–1370, <https://doi.org/10.1002/2014GB004888>, 2014.
- 930 Hassoun, A. E. R., Gemayel, E., Krasakopoulou, E., Goyet, C., Abboud-Abi Saab, M., Ziveri, P., Touratier, F., Guglielmi, V. and Flaco, C.: Modeling of the Total Alkalinity and the Total Inorganic Carbon in the Mediterranean Sea, *Journal of Water Resources and Ocean Science*, 4(1), 24-32, <https://doi.org/10.11648/j.wros.20150401.14>, 2015.
- Hopkins, T. S.: The structure of Ionian and Levantine Seas, *Rep. Meteorol. Oceanogr.*, 41(II), pp. 35 – 56, Harvard Univ., Cambridge, Mass, 1992.
- 935 Ingrosso, G., Giani, M., Cibic, T., Karuza, A., Kralj, M. and Del Negro, P.: Carbonate chemistry dynamics and biological processes along a river–sea gradient (Gulf of Trieste, northern Adriatic Sea), *Journal of Marine Systems*, 155, 35-49, <https://doi.org/10.1016/j.jmarsys.2015.10.013>, 2016.
- Kapsenberg, L., Alliouane, S., Gazeau, F., Mousseau, L. and Gattuso, J. -P.: Concomitant Ocean acidification and increasing total alkalinity at a coastal site in the NW Mediterranean Sea (2007-2015), *Ocean Science*, 13, 411-426, <https://doi.org/10.5194/os-13-411-2017>, 2017.
- 940 Krumins, V., Gehlen, M., Arndt, S., Van Cappellen, P. and Regnier, P.: Dissolved inorganic carbon and alkalinity fluxes from coastal marine sediments: Model estimates for different shelf environments and sensitivity to global change, *Biogeosciences*, 10, 371–398, <https://doi.org/10.5194/bg-10-371-2013>, 2013.
- 945 Kwiatkowski, L. and Orr, J. C.: Diverging seasonal extremes for ocean acidification during the twenty-first century, *Nature Climate Change*, 8(2), 141-145, <https://doi.org/10.1038/s41558-017-0054-0>, 2018.
- Lajaunie-Salla, K., Diaz, F., Wimart-Rousseau, C., Wagener, T., Lefevre, D., Yohia, C., Xueref-Remy, I., Nathan, B., Armengaud, A., and Pinazo, C.: Implementation and assessment of a carbonate system model (Eco3m-CarbOx v1.1) in a highly dynamic Mediterranean coastal site (Bay of Marseille, France), *Geoscience Model Development*, 14, 295–321, <https://doi.org/10.5194/gmd-14-295-2021>, 2021.
- 950

- Laruelle, G. G., Dürr, H. H., Slomp, C. P. and Borges, A. V.: Evaluation of sinks and sources of CO₂ in the global coastal ocean using a spatially explicit typology of estuaries and continental shelves, *Geophysical Research Letters*, 37, L15607, <https://doi.org/10.1029/2010GL043691>, 2010.
- Laruelle, G. G., Lauerwald, R., Pfeil, B. and Regnier, P.: Regionalized global budget of the CO₂ exchange at the air-water interface in continental shelf seas, *Global Biogeochemical Cycles*, 28-11, 1199-1214, <https://doi.org/10.1002/2014GB004832>, 2014.
- Lewis, E. and Wallace, D. W. R.: Program developed for CO₂ system calculations, 1998.
- Lovenduski, N. S., Gruber, N., Scott, C. D. and Lima, I. D.: Enhanced CO₂ outgassing in the Southern Ocean from a positive phase of the Southern Annular Mode, *Global Biogeochemical Cycles*, 21, <https://doi.org/10.1029/2006GB002900>, 2007.
- 955 Luchetta, A., Cantoni, C. and Catalano, G.: New observations of CO₂-induced acidification in the northern Adriatic Sea over the last quarter century. *Chemistry and Ecology*, 26, 1-17, <https://doi.org/10.1080/02757541003627688>, 2010.
- Ludwig, W. E., Dumont, M., Meybeck, M. and Heussner, S.: River discharges of water and nutrients to the Mediterranean and Black Sea: Major drivers for ecosystem changes during past and future decades? *Progress in Oceanography*, 80(3-4), 199–217, <https://doi.org/10.1016/j.pocean.2009.02.001>, 2009.
- 965 Lueker, T. J., Dickson, A. G. and Keeling, C. D.: Ocean pCO₂ calculated from dissolved inorganic carbon, alkalinity, and equations for K₁ and K₂: Validation based on laboratory measurements of CO₂ in gas and seawater at equilibrium, *Marine Chemistry*, 70, 105–119, [https://doi.org/10.1016/S0304-4203\(00\)00022-0](https://doi.org/10.1016/S0304-4203(00)00022-0), 2000.
- Maréchal, D.: A soil-based approach to rainfall-runoff modelling in ungauged catchments for England and Wales, Ph.D. Thesis, Cranfield University, 157pp, 2004.
- 970 Middelburg, J. J.: Marine carbon biogeochemistry, A primer for earth system scientists, Springer Briefs in Earth System Sciences, Springer Nature Switzerland AG, Cham, Switzerland, 2019.
- Middelburg, J. J., Soetaert, K. and Hagens, M.: Ocean alkalinity buffering and biogeochemical processes, *Reviews of Geophysics*, 58 (3), e2019RG000681, <https://doi.org/10.1029/2019RG000681>, 2020.
- Millet, B., Pinazo, C., Banaru, D., Pagès, R., Guiart, P. and Pairaud, I.: Unexpected spatial impact of treatment plant discharges induced by episodic hydrodynamic events: Modelling lagrangian transport of fine particles by Northern Current intrusions in the Bays of Marseille (France), *Édité par João Miguel Dias, PLoS ONE*, 13 (4), <https://doi.org/10.1371/journal.pone.0195257>, 2018.
- 975 Millero, F. J.: Thermodynamics of the carbon dioxide system in the oceans, *Geochimica Cosmochimica Acta*, 59, 661–677, [https://doi.org/10.1016/0016-7037\(94\)00354-O](https://doi.org/10.1016/0016-7037(94)00354-O), 1995.
- 980 Millot, C.: The Golf of Lions' hydrodynamic, *Continental Shelf Research*, 10, 885-894, 1990.
- Morel, A. and André, J. -M.: Pigment distribution and primary production in the western Mediterranean as derived and modelled from coastal zone colour scanner observations, *96(C7)*, 12685-12698, <https://doi.org/10.1029/91JC00788>, 1991.
- Morris, A. W. and Riley, J. P.: The bromide/chlorinity and sulphate/ chlorinity ratio in sea water, *Deep-Sea Research*, 13, 699-705, 1966.

- 985 Mucci, A.: The solubility of calcite and aragonite in seawater at various salinities, temperatures, and one atmosphere total pressure, *American Journal of Science*, 283, 780–799, <https://doi.org/10.2475/ajs.283.7.780>, 1983.
- Orr, J. C., Fabry, V. J., Aumont, O., Bopp, L., Doney, S. C., Feely, R. A., Gnanadesikan, A., Gruber, N., Ishida, A. and Joos, F.: Anthropogenic Ocean acidification over the twenty-first century and its impact on calcifying organisms, *Nature*, 437(7059), 681-686, <https://doi.org/10.1038/nature04095>, 2005.
- 990 Pairaud, I., Gatti, J., Bensoussan, N., Verney, R., and Garreau, P.: Hydrology and circulation in a coastal area off Marseille: Validation of a nested 3D model with observations, *J. Marine Syst.*, 88, 20–33, <https://doi.org/10.1016/j.jmarsys.2011.02.010>, 2011.
- Pont, D., Simonnet, J.-P., and Walter, A. V.: Medium-term changes in suspended sediment delivery to the Ocean: Consequences of catchment heterogeneity and river management (Rhône River, France), *Estuarine, Coastal and Shelf Science*, 54, 1–18, <https://doi.org/10.1006/ecss.2001.0829>, 2002.
- 995 Pujon-Pay, M., Conan, P., Joux, F., Oriol, L., Naudin, J. -J. and Cauwet, G.: Impact of phytoplankton and bacterial production on nutrient and DOM uptake in the Rhône River plume (NW Mediterranean), *Marine Ecology Progress Series*, 315, 43-54, <https://doi.org/10.3354/meps315043>, 2006.
- Radach, G. and Moll, A.: Review of three-dimensional ecological modelling related to the North Sea shelf system. Part II: model validation and data needs, *Oceanography and Marine Biology*, 44, 1–60, 2006.
- 1000 Revelante, N. and Gilmartin, M.: The effect of Po River discharge on phytoplankton dynamics in the Northern Adriatic Sea, *Marine Biology*, 34, 259-271, <https://doi.org/10.1007/BF00388803>, 1976.
- Riley, J. P.: The occurrence of anomalously high fluoride concentrations in the North Atlantic, *Deep-Sea Research* 12, 219-220, 1965.
- 1005 Riley, J. P. and Tongudai. M.: The major cation/chlorinity ratios in sea water, *Chemical Geology*, 2, 263-269, 1967.
- Roobaert, A., Laruelle, G. G., Landschützer, P., Gruber, N., Chou, L. and Regnier, P.: The Spatiotemporal Dynamics of the Sources and Sinks of CO₂ in the Global Coastal Ocean, *Global Biogeochemical Cycles*, 33, 1693-1714, <https://doi.org/10.1029/2019GB006239>, 2019.
- Ross, O. N., Frayssé, M., Pinazo, C. and Pairaud, I.: Impact of an intrusion by the Northern Current on the biogeochemistry in the Eastern Gulf of Lion, NW Mediterranean, *Estuarine, Coastal and Shelf Science*, 170, 1-9, 2016.
- 1010 Salat, J., Garcia, M. A., Cruzado, A., Palanques, A., Arin, L., Gomis, D., Guillen, J., De Leon, A., Puigdefàbregas, J., Sospedra, J. and Velasquez, Z. R.: Seasonal changes of water mass structure and shelf slope exchanges at the Ebro Shelf (NW Mediterranean), *Continental Shelf Research*, 22, pp. 327-348, [https://doi.org/10.1016/S0278-4343\(01\)00031-0](https://doi.org/10.1016/S0278-4343(01)00031-0), 2002.
- Schaeffer, A., Molcard, A., Forget, P., Fraunié, P. and Garreau, P.: Generation mechanisms for mesoscale eddies in the Gulf of Lions: radar observation and modelling, *Ocean Dynamics*, 61, 1587-1609, <https://doi.org/10.1007/s10236-011-0482-8>, 2011.
- 1015 Schneider, A., Douglas, W. R. W. and Körtzinger, A.: Alkalinity of the Mediterranean Sea, *Geophysical Research Letters*, 34, <https://doi.org/10.1029/2006GL028842>, 2007.

- Sempere, R., Charrière, B., Van Wambeke, F. and Cauwet, G.: Carbon inputs of the Rhône River to the Mediterranean Sea: Biogeochemical implications, *Global Biogeochemical Cycles*, American Geophysical Union, 14(2), 669-681, <https://doi.org/10.1029/1999GB900069>, 2000.
- Sharp, J. D., Pierrot, D., Humpbreys, M. P., Epitalon, J. -M., Orr, J. C., Lewis, E. R. and Wallace, D. W. R.: CO2SYSv3 for MATLAB (v3.0.1). Zenodo [code] <https://doi.org/10.5281/zenodo.3952803>, 2020.
- Stow, C. A., Jolliff, J., McGillicuddy Jr, D. J., Doney, S. C., Allen, J. I., Friedrichs, M. A., Rose, K. A. and Wallhead, P.: Skill assessment for coupled biological/physical models of marine systems, *Journal of Marine Systems*, 76(1-2), 4-15, <https://doi.org/10.1016/j.jmarsys.2008.03.011>, 2009.
- Thomas, H., Bozec, Y., Elkalay, K. and De Baar, H. J. W.: Enhanced Open Ocean Storage of CO₂ from Shelf Sea Pumping, *Science*, 304-5673, 1005-1008, <https://doi.org/10.1126/science.1095491>, 2004.
- Turi, G., Lachkar, Z. and Gruber, N.: Spatiotemporal variability and drivers of pCO₂ and air-sea CO₂ fluxes in the California Current System: an eddy-resolving modeling study, *Biogeosciences*, 11, 671-690, <https://doi.org/10.5194/bg-11-671-2014>, 2014.
- Uppstrom, L. R.: The boron/chlorinity ratio of deep-sea water from the Pacific Ocean, *Deep-Sea Research*, 21, 161-162, 1974.
- Urbini, L., Ingrosso, G., Djakovac, T., Piacentino, S. and Giani, M.: Temporal and Spatial Variability of the CO₂ System in a Riverine Influenced Area of the Mediterranean Sea, the Northern Adriatic, *Frontiers in Marine Science*, 7-679, <https://doi.org/10.3389/fmars.2020.00679>, 2020.
- Van Slyke, D. D.: On the measurement of buffer values and on the relationship of buffer value to the dissociation constant of the buffer and the concentration and reaction of the buffer solution, *Journal of Biological Chemistry*, 52, 525-570, 1922.
- Wanninkhof, R.: Relationship between wind speed and gas exchange over the ocean revisited, *Limnology and Oceanography: Methods*, 12 (6), 351-362, <https://doi.org/10.4319/lom.2014.12.351>, 2014.
- Weiss, R. F.: Carbon dioxide in water and seawater: The solubility of a non-ideal gas, *Marine Chemistry*, 2(3), 203-215, [https://doi.org/10.1016/0304-4203\(74\)90015-2](https://doi.org/10.1016/0304-4203(74)90015-2), 1994.
- Wimart-Rousseau, C., Lajaunie-Salla, K., Marrec, P., Wagener, T., Raimbault, P., Lagadec, V., Lafont, M., Garcia, N., Diaz, F., Pinazo, C., Yohia, C., Garcia, F., Xueref-Remy, I., Blanc, P. E., Armengaud, A., and Lefèvre, D.: Temporal variability of the carbonate system and air-sea CO₂ exchanges in a Mediterranean human-impacted coastal site, *Estuar. Coast. Shelf S.*, 236, <https://doi.org/10.1016/j.ecss.2020.106641>, 2020.
- Wolf-Gladrow, D. A., Zeebe, R. E., Klaas, C., Körtzinger, A. and Dickson, A. G.: Total Alkalinity: The explicit conservative expression and its application to biogeochemical processes, *Marine Chemistry*, 106, 287-300, <https://doi.org/10.1016/j.marchem.2007.01.006>, 2007.
- Yohia, C.: Genèse du mistral par interaction barocline et advection du tourbillon potentiel, *Climatologie*, 13, 24-37, <https://doi.org/10.4267/climatologie.1182>, 2017.